J. Fluid Mech. (2010), *vol.* 659, *pp.* 318–350.
doi:10.1017/S0022112010002491

Stability of pressure-driven flow in a deformable neo-Hookean channel

GAURAV AND V. SHANKAR†

Department of Chemical Engineering, Indian Institute of Technology, Kanpur 208 016, India

(Received 26 September 2009; revised 23 April 2010; accepted 23 April 2010;
first published online 9 July 2010)

The stability of pressure-driven flow in a rectangular channel with deformable neo-Hookean viscoelastic solid walls is analysed for a wide range of Reynolds numbers (from $Re \ll 1$ to $Re \gg 1$) by considering both sinuous and varicose modes for the perturbations. Pseudospectral numerical and asymptotic methods are employed to uncover the various unstable modes, and their stability boundaries are determined in terms of the solid elasticity parameter $\Gamma = V\eta/(ER)$ and the Reynolds number $Re = RV\rho/\eta$; here V is the maximum velocity of the laminar flow, R is the channel half-width, η and ρ are respectively the viscosity and density of the fluid and E is the shear modulus of the solid layer. We show that for small departures from a rigid solid, wall deformability could have a destabilizing or stabilizing effect on the Tollmien–Schlichting (TS) instability (a sinuous mode) depending on the solid-layer thickness. Upon further increase in solid deformability, the TS mode coalesces with another unstable mode (absent in rigid channels) giving rise to a single unstable mode which extends to very low Reynolds number (<1) for highly deformable walls. There are other types of instabilities that exist only due to wall deformability. In the absence of inertia ($Re = 0$), there is a short-wave instability of both sinuous and varicose modes arising due to the discontinuity of the first normal stress difference across the fluid–solid interface. For both sinuous and varicose modes, it is shown that inclusion of inertia is important even for $Re \ll 1$, wherein a new class of long-wavelength unstable modes are predicted which are absent at $Re = 0$. These unstable modes are a type of shear waves in an elastic solid which are destabilized by the flow. These long- and short-wave instabilities are absent if a simple linear elastic model is used for the solid. At intermediate and high Re, upstream and downstream travelling waves of both sinuous and varicose modes become unstable. We show that sinuous and varicose modes become critical in different parameter regimes, thereby demonstrating the importance of capturing all the unstable modes. Inclusion of dissipative effects in the neo-Hookean model is generally shown to play a stabilizing role on the instabilities due to both sinuous and varicose modes. The predicted instabilities will be important for the flow of liquids (with viscosity $\geqslant 10^{-3}$ Pa s) in deformable channels of width $\leqslant 1$ mm, and with shear modulus $\leqslant 10^5$ Pa.

Key words: elastic waves, flow vessel interactions, instability

1. Introduction

Fluid flow through channels made of deformable walls is encountered in a wide class of biological systems (Grotberg & Jensen 2004) and more recently in microfluidic

† Email address for correspondence: vshankar@iitk.ac.in

applications (Squires & Quake 2005). Owing to their small dimensions, the Reynolds number of fluid flow in microfluidic devices is often $O(1)$ or smaller. At such low Reynolds number, flow in rigid-walled channels and tubes is laminar and has poor mixing characteristics, which is a major limitation in the design of microfluidic devices. Turbulent flows with better mixing characteristics often ensue as a result of an instability of the laminar flow, which occurs in rigid-walled channels only at large Reynolds numbers of $O(10^3)$. In contrast, for flows in channels with deformable walls, the elasticity of the solid wall also plays a role in destabilizing the flow in addition to fluid inertia (Krindel & Silberberg 1979). Because of the deformation of the solid interface by fluid stresses, the stability of the flow could be altered due to the creation of interfacial waves thereby leading to a complicated time-dependent flow in such systems. The resulting unsteady, non-laminar flows have better mixing characteristics compared to laminar flows, and could result in improved heat and mass transfer rates in microfluidic devices. A recent experimental work by Shrivastava, Cussler & Kumar (2008) has found evidence for enhancement of mass transfer due to a hydrodynamic instability induced by a soft elastic boundary. This feature could be potentially exploited in improving mixing in microfluidic devices fabricated using 'soft' platforms like polydimethyl siloxane (PDMS) (McDonald & Whitesides 2002; Squires & Quake 2005), which can be tailor-made with desired elastic properties. To this end, it is important to have a precise quantitative understanding of the onset of instability of the laminar flow in deformable channels as a function of the elastic modulus of the channel walls. There has also been enormous interest in the stability of flow past deformable solids at higher Reynolds numbers of $O(10^3)$, wherein soft solid coatings were investigated as potential candidates for delay of the Tollmien–Schlicting (TS) instability present in flow past rigid walls (see Gad-el-Hak 2003 for a recent review). The boundary-layer flow is the most studied configuration in this context owing to its practical relevance. However, the TS instability is also present in pressure-driven flow in a rigid channel, and a study on the effect of wall deformability on flow in this simpler geometry with a truly parallel laminar velocity profile will lead to a better understanding of the role of deformable walls on the TS instability. With these main motivations, we present a comprehensive study of the stability characteristics of fully developed pressure-driven flow in a rectangular channel whose walls are lined with deformable solid layers for Reynolds numbers ranging from $Re \ll 1$ to $Re \gg 1$, by considering both sinuous and varicose modes for the perturbations. The overall objective is to investigate the existence of qualitatively new instabilities in regimes that have not been addressed thus far in the literature. Below, we first give a brief account of relevant earlier work on this subject, and motivate the importance of the present work in the context of the existing literature.

2. Background and earlier work

The stability of pressure-driven flow in a deformable channel has been addressed in many previous studies (Hains & Price 1962; Green & Ellen 1972; Rotenberry & Saffman 1990; Gajjar & Sibanda 1996; Davies & Carpenter 1997; LaRose & Grotberg 1997; Huang 1998), and the focus of these earlier studies was on the effect of solid deformability on the TS instability. Prior to these studies, Benjamin (1960) and Landahl (1962) pioneered the research on the stability of flow past compliant surfaces by focusing on boundary-layer flow over a compliant wall. These studies employed a thin spring-backed membrane as a model for the deformable solid where the deflection of the wall is governed by an equation that is linear in the forcing

due to fluid stresses. At a Reynolds number of 5771, fully developed plane Poiseuille flow in a rigid channel becomes linearly unstable due to the TS instability (Drazin 2002). Hains & Price (1962) first showed that wall flexibility has a stabilizing effect on the TS instability in a rigid channel. Green & Ellen (1972) showed numerically that for sufficiently deformable walls the neutral stability curve for the TS mode could be significantly affected such that an additional region of instability (subsequently identified as 'travelling wave flutter') appears at higher wavenumbers. Gajjar & Sibanda (1996) studied the stability of flow in a channel with one rigid wall and one flexible wall, and showed that the effect of wall damping is destabilizing on the TS mode. Their analysis further pointed to another instability called flutter, which is absent in rigid surfaces. Davies & Carpenter (1997) carried out a detailed study on the stability of channel flow, and showed that in addition to the TS instability, there exists a class of 'flow-induced surface instabilities' which are modes that are destabilized by wall flexibility, and are absent in rigid channels. They also showed that the TS mode and the flow-induced surface instabilities interact in certain parametric regimes to give rise to a powerful possibly absolute instability. Davies & Carpenter (1997), however, considered only sinuous modes that have the same symmetry as the TS modes. Huang (1998) considered varicose modes and reported a new inviscid flow-induced surface instability. Nagata & Cole (1999) studied both sinuous and varicose modes of instabilities in a symmetric flexible-walled channel. LaRose & Grotberg (1997) studied the stability of developing flow in a flexible channel, and predicted a new long-wave instability and a finite-wavelength flutter instability. Very recently, Stewart, Walters & Jensen (2010) and Mandre & Mahadevan (2010) have studied new types of instabilities in the flow between a rigid wall and a tensioned membrane. An important limitation of all these studies is that the channel walls were constrained to move only in normal direction. In addition, it is difficult to relate the phenomenological parameters in the model to measurable material properties of a solid such as the shear modulus.

Yeo (1988) used a continuum linear viscoelastic solid of finite thickness as a model for the deformable wall to analyse the stability of laminar boundary-layer flow over a deformable wall. It was shown there that the TS mode is stabilized by increase in wall deformability, but this also introduces a host of new instabilities. Using a continuum linear viscoelastic model for the deformable wall, Kumaran and co-workers (Kumaran 1995, 1998; Srivatsan & Kumaran 1997; Shankar & Kumaran 2001) have extensively analysed the stability of pressure-driven flow in a circular pipe which is lined by a linear viscoelastic material, as well as plane Couette flow past a linear viscoelastic solid. However, it has recently been pointed out (Gkanis & Kumar 2003, 2005) that in order to accurately capture the stability behaviour in flow past deformable solids, it is necessary to use a frame-indifferent nonlinear continuum model for the solid. Even earlier, Yeo, Khoo & Chong (1994) have similarly pointed out the inconsistencies associated with the linear elastic model in the context of boundary-layer stability, by using a neo-Hookean model for the solid. Gkanis & Kumar (2005) considered the problem of stability of plane Poiseuille flow in a deformable channel in the creeping-flow limit using the neo-Hookean model, but considered only varicose perturbations. They showed that for pressure-driven flow, there are two types of instability for $Re = 0$: (i) a finite-wavelength mode which becomes unstable for thicker solids, and which is akin to the instability found for plane Couette flow (Gkanis & Kumar 2003), and (ii) a short-wavelength mode that arises due to the discontinuity of the first normal stress difference in the solid–fluid interface in the base state. We demonstrate

in § 3.4 that their formulation of the tangential and normal stress conditions needs a minor modification relating to the treatment of the stress continuity conditions at the perturbed interface when the solid is treated within a Lagrangian description. In addition, the work of Gkanis & Kumar (2005) was restricted to creeping-flow limit ($Re = 0$), and to purely elastic neo-Hookean solids. Their analysis also considered only varicose perturbations.

The present study complements the work of Gkanis & Kumar (2005) by removing all the above restrictions, by extending their results to (i) both sinuous and varicose perturbations, (ii) finite and high Re and (iii) viscoelastic neo-Hookean solids. Consideration of perturbations with both the symmetries is essential for experimental comparisons. Further, inertial effects, however small, will always be present in real systems and it is instructive to examine the effect of inertia on the stability of pressure-driven flow in deformable channels. For non-zero Reynolds number, the characteristic equation for the coupled fluid–solid system admits multiple solutions for the eigenvalue, and it is possible that some of these solutions may become unstable in addition to the creeping-flow modes: there could be unstable modes for $Re \ll 1$ which cannot be captured by setting $Re = 0$. Physically, the additional modes at small but non-zero Re correspond to a class of shear waves in a solid (Achenbach 1973) which could be modified and destabilized by the fluid flow. Even at $Re \gg 1$, there exist multiple downstream and upstream travelling waves which become unstable in flow through deformable tubes and channels (Shankar & Kumaran 2001, 2002; Gaurav & Shankar 2009). Finally, real elastomers and polymer gels usually exhibit some viscous dissipation upon deformation, and it is important to include this aspect in the constitutive model for the solid. The present work also supplements the earlier studies on the role of wall deformability on the TS instability in a channel (Hains & Price 1962; Gajjar & Sibanda 1996; Davies & Carpenter 1997), by considering a more realistic neo-Hookean model for the solid to address the role of solid deformability on the stability of the TS mode.

The rest of this paper is structured as follows: the base state, linearized equations governing the stability of the system and boundary conditions are presented in § 3. The results of the analysis in various regimes are discussed in § 4 and finally the conclusions of the present study are given in § 5. Appendices A and B provide details concerning linearization of conditions at the fluid–solid interface and the low-wavenumber low-Re asymptotic analysis.

3. Problem formulation

3.1. *Governing equations for the fluid and solid*

We consider the pressure-driven flow of an incompressible Newtonian fluid of density ρ and viscosity η in a rectangular channel lined with a deformable solid layer as shown in figure 1. The solid layer is of thickness HR and is strongly bonded to rigid surface at $z^* = R(2 + H)$ on top and $z^* = -HR$ at bottom, and the fluid occupies the region $0 \leqslant z^* \leqslant 2R$ in the base state. The deformable solid is modelled as an impermeable and incompressible neo-Hookean (Malvern 1969; Holzapfel 2000) viscoelastic solid of density ρ, shear modulus E and viscosity η_s. Various physical quantities are non-dimensionalized at the outset by using the following scales: R for lengths and deformations, the maximum base flow velocity V for velocities and $\eta V/R$ for pressure and stresses. The steady fully developed velocity profile whose stability is of interest

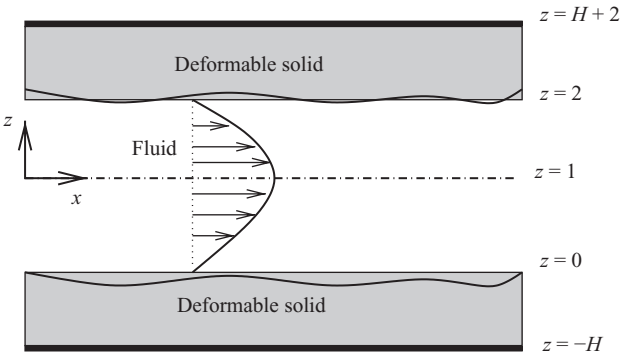

FIGURE 1. Schematic diagram showing the configuration and (non-dimensional) coordinate system considered in this paper: pressure-driven flow of a Newtonian fluid in a channel lined with neo-Hookean viscoelastic solid.

is the pressure-driven flow inside the channel

$$\overline{v}_x(z) = 2\left(z - \frac{z^2}{2}\right), \qquad \overline{v}_z = 0. \tag{3.1}$$

The non-dimensional governing equations for the fluid are Navier–Stokes continuity and momentum balance equations:

$$\nabla \cdot \boldsymbol{v} = 0, \qquad Re[\partial_t \boldsymbol{v} + \boldsymbol{v} \cdot \nabla \boldsymbol{v}] = -\nabla p + \nabla^2 \boldsymbol{v}, \tag{3.2}$$

where $\boldsymbol{v}$ and p are the velocity and pressure fields in the fluid layer and $Re = \rho V R/\eta$ is the Reynolds number based on maximum fluid velocity.

The governing equations for the fluid are written, as is customary, in terms of spatial (Eulerian) coordinates ($\boldsymbol{x} = x, y, z$). It is possible to express the dynamical quantities and governing equations in the solid also in a consistent Eulerian fashion (Chokshi 2007; Choskshi & Kumaran 2008). Equivalently (following Gkanis & Kumar 2003), we find it convenient to refer the governing equations for the solid in terms of a reference (Lagrangian) configuration, where the independent variables are the positions $\boldsymbol{X} = (X, Y, Z)$ of material particles in the reference (i.e. unstressed solid) configuration. Chokshi (2007) has shown that the Eulerian–Eulerian and Eulerian–Lagrangian approaches are equivalent, and yield the same result for the eigenvalues. In a recent work, Ma & Ng (2009) have used an entirely Lagrangian approach for both the fluid and solid to analyse the propagation of waves in an elastic tube, when there is no base flow in the fluid. However, their approach is not easily applicable to the case when there is a base flow in the fluid, as is the case in this study.

The spatial (x, y, z) coordinate system used here for fluid motion is identical to the reference coordinate system in the unstressed configuration (X, Y, Z) for the deformable solid. In the deformed state of the solid, the current position of a material particle is denoted in the Lagrangian description by $\boldsymbol{w}(\boldsymbol{X})$. The deformable solid is modelled as an incompressible neo-Hookean viscoelastic solid and the mass and momentum conservation equations governing the dynamics of solid are given as (Malvern 1969; Holzapfel 2000):

$$\det(\boldsymbol{F}) = 1, \tag{3.3}$$

$$Re\left[\frac{\partial^2 \boldsymbol{w}}{\partial t^2}\right]_{\boldsymbol{X}} = \nabla_{\boldsymbol{X}} \cdot \boldsymbol{P}. \tag{3.4}$$

In the above equations, $\boldsymbol{F}$ is the deformation gradient tensor defined as $\boldsymbol{F} = \nabla_X \boldsymbol{w}$ and $\boldsymbol{P}$ is the first Piola–Kirchhoff stress tensor. The first Piola–Kirchhoff stress tensor is related to Cauchy stress tensor by $\boldsymbol{P} = \boldsymbol{F}^{-1} \cdot \boldsymbol{\sigma}$. The Cauchy stress tensor for the neo-Hookean viscoelastic solid is split into an elastic part, $\boldsymbol{\sigma}^e$, and a dissipative part, $\boldsymbol{\sigma}^d$ (Beatty & Zhou 1991; Fosdick & Yu 1996; Destarde & Saccomandi 2004; Ma & Ng 2009):

$$\boldsymbol{\sigma} = \boldsymbol{\sigma}^e + \boldsymbol{\sigma}^d, \tag{3.5}$$

$$\boldsymbol{\sigma}^e = -p_s \boldsymbol{I} + \frac{1}{\Gamma} \boldsymbol{F} \cdot \boldsymbol{F}^T, \quad \boldsymbol{\sigma}^d = \eta_r (\boldsymbol{L} + \boldsymbol{L}^T). \tag{3.6}$$

Here, the non-dimensional parameter $\Gamma = V\eta/(ER)$ is the ratio of viscous stress in the fluid to elastic stresses in the solid, and signifies the extent of deformability of the solid. If $\Gamma \to 0$, this represents the limit of a rigid solid layer, and as Γ increases, the solid becomes more deformable; p_s is the pressure-like function related to actual pressure, $\hat{p}_s$, in the neo-Hookean solid as $p_s = \hat{p}_s + 1/\Gamma$; $\boldsymbol{L} = \dot{\boldsymbol{F}} \cdot \boldsymbol{F}^{-1}$ is the spatial velocity gradient and $\eta_r = \eta_s/\eta$ is the ratio of solid to fluid viscosity. To simplify our calculations, we assume a frequency-independent viscosity to describe dissipative effects in the solid medium. The neutral stability curves obtained in the present study can be extended to a solid with frequency-dependent viscosity by following an iterative procedure described in Muralikrishnan & Kumaran (2002). A simple single-mode Maxwellian model for the viscoelastic response of the solid has been used in Choskshi & Kumaran (2008). In the above governing equations for solid layer, the density of the solid is assumed to be equal to the fluid density because the densities of commonly used polymeric materials are usually not very different from those of various liquids. Thus, the ratio of solid to fluid density ρ_s/ρ will be close to one and for small differences in densities we expect that the qualitative prediction of the present study will remain unchanged. However, for $\rho_s/\rho \ll 1$ or $\gg 1$, the density differences could modify the modes explored in the present study and may introduce new modes of instabilities.

When numerical results are presented later in this work, it is often convenient to express how the Reynolds number required for instability varies as the deformability of the solid wall is changed. To this end, we will mainly use the variation of Γ as a function of Re. We will also display some of our results in the form of Re as a function of $\Sigma = Re/\Gamma = \rho E R^2/\eta^2$, which illustrates how a flow-dependent quantity (Re) varies as a function of a flow-independent quantity (Σ) which measures how rigid the solid is. For a truly rigid solid, $\Sigma \to \infty$.

3.2. *Base state*

In the base state, the fluid–solid interface is flat and unperturbed, and is denoted in the Eulerian description by $x, z = 0$, and in the Lagrangian description by $X, Z = 0$. Upon introduction of perturbations to the system, the interface is described in the Eulerian description by $x, z = h(x)$, while a material point on the interface is still labelled in the Lagrangian description by $X(x), Z = 0$. The boundary conditions at the fluid–solid interface (denoted by $z = h(x)$ in the Eulerian scheme, or by $X, Z = 0$ in the Lagrangian scheme) are continuity of velocities and stresses. At $Z = -H$, the deformable solid wall is fixed onto a rigid surface and hence the boundary conditions are those of no deformations ($\boldsymbol{w} = 0$) at the rigid surface. The steady-state base velocity profile for fluid and the base-state deformation field for solid layers are obtained by solving the governing equations (3.2) and (3.3)–(3.4) respectively, along

with the appropriate boundary conditions. The base velocity profile in a fluid layer is given by (3.1). The fluid–solid interface ($Z=0$) remains flat and the solid is at rest with a non-zero displacement in x direction due to shear stress exerted by fluid at the fluid–solid interface. The steady base deformation and pressure fields for a deformable solid layer (in the domain $-H<Z<0$) are given by

$$\overline{w}_X = X + \Gamma[H^2 - Z^2] + 2\Gamma(Z+H), \quad \overline{w}_Z = Z, \tag{3.7}$$

$$\overline{p}_s = \overline{p}(X) + 4\Gamma\left(\frac{Z^2}{2} - Z\right), \tag{3.8}$$

where the overbar denotes various base-state physical quantities. The neo-Hookean solid also exhibits a first normal stress difference in the base state: $\sigma_{XX}-\sigma_{ZZ}=4\Gamma(Z-1)^2$, which is known to give rise to a short-wave instability (Gkanis & Kumar 2003).

3.3. *Linearized governing equations*

The temporal linear stability of the system is studied by imposing small perturbations to the base state and linearizing the resulting governing equations and boundary conditions about the base-state solution. Following previous work on channel flows, the perturbations are assumed to be two-dimensional. In the study of rigid channel flows, this is normally justified within the classical eigenvalue-oriented analysis by invoking Squire's theorem (Drazin & Reid 1981) which states that two-dimensional perturbations are the most unstable. However, it is not possible to derive a Squire's theorem for deformable channels, and it is in principle possible for three-dimensional perturbations to be more unstable for these systems. The two-dimensional perturbations are expressed using the normal mode decomposition as: $f' = \tilde{f}(z)\exp[\mathrm{i}k(x-ct)]$ for fluid perturbation quantities and $f' = \tilde{f}(Z)\exp[\mathrm{i}k(X-ct)]$ for solid quantities, where f' is the perturbation to any physical variable, $\tilde{f}(z)$ is the complex amplitude (eigenfunction) of the disturbance, k is the (real) streamwise wavenumber of perturbations and $c=c_r+\mathrm{i}c_i$ is the complex wave speed. If $c_i>0$ (or $c_i<0$), flow will be unstable (or stable). In this connection, it must be noted that a stability analysis based only on the eigenvalues does not always yield a complete picture of the system's stability. The conclusions based on the individual eigenvalues are only related to the long-time asymptotic growth or decay of perturbations. It is possible that the flow could experience transient growth (Schmid & Henningson 2001; Schmid 2007) at a Reynolds number lower than that predicted in our analysis due to the underlying non-normality of the differential operators. However, the inclusion of non-normal effects is beyond the scope of the present work.

The linearized governing equations for fluid layers are

$$\mathrm{d}_z\tilde{v}_z + \mathrm{i}k\tilde{v}_x = 0, \tag{3.9}$$

$$Re[\mathrm{i}k\tilde{v}_x(\overline{v}_x - c) + \tilde{v}_z(\mathrm{d}_z\overline{v}_x)] = -\mathrm{i}k\tilde{p} + \left(\mathrm{d}_z^2 - k^2\right)\tilde{v}_x, \tag{3.10}$$

$$Re[\mathrm{i}k(\overline{v}_x - c)\tilde{v}_z] = -\mathrm{d}_z\tilde{p} + \left(\mathrm{d}_z^2 - k^2\right)\tilde{v}_z. \tag{3.11}$$

In the following, the terms enclosed in boxes in the linearized governing equations for deformable solid (3.12)–(3.14) and in the interfacial conditions (3.17)–(3.18) represent the different couplings between the base state and perturbation variables that arise due to the nonlinearities present in the constitutive relation for neo-Hookean viscoelastic solid. These boxed terms will be absent if the solid layer is modelled as a linear

viscoelastic solid. The linearized equations for solid layers are

$$\frac{\mathrm{d}\tilde{w}_Z}{\mathrm{d}Z} + \mathrm{i}k\tilde{w}_X + \boxed{2\mathrm{i}k\Gamma(Z-1)\tilde{w}_Z} = 0, \tag{3.12}$$

$$\boxed{2\frac{\mathrm{d}\tilde{w}_Z}{\mathrm{d}Z} + 4\mathrm{i}k\Gamma(Z-1)\tilde{w}_Z} - \mathrm{i}k\tilde{p}_s + \left(\frac{1}{\Gamma} - \mathrm{i}kc\eta_r\right)\left(\frac{\mathrm{d}^2}{\mathrm{d}Z^2} - k^2\right)\tilde{w}_X$$
$$+ \mathrm{i}kc\eta_r \boxed{\left(4k^2\Gamma^2(Z-1)^2\tilde{w}_X + 4\mathrm{i}k\Gamma(1-Z)\frac{\mathrm{d}\tilde{w}_X}{\mathrm{d}Z} - 2\mathrm{i}k\Gamma\tilde{w}_X\right)} = -k^2c^2Re\,\tilde{w}_X, \tag{3.13}$$

$$\boxed{-2\frac{\mathrm{d}\tilde{w}_X}{\mathrm{d}Z} + 2\mathrm{i}k\Gamma(1-Z)\tilde{p}_s - 4\mathrm{i}k\Gamma(Z-1)\tilde{w}_X}$$
$$-\frac{\mathrm{d}\tilde{p}_s}{\mathrm{d}Z} + \left(\frac{1}{\Gamma} - \mathrm{i}kc\eta_r\right)\left(\frac{\mathrm{d}^2}{\mathrm{d}Z^2} - k^2\right)\tilde{w}_Z$$
$$+ \mathrm{i}kc\eta_r \boxed{\left(4k^2\Gamma^2(Z-1)^2\tilde{w}_Z + 4\mathrm{i}k\Gamma(1-Z)\frac{\mathrm{d}\tilde{w}_Z}{\mathrm{d}Z} - 2\mathrm{i}k\Gamma\tilde{w}_Z\right)} = -k^2c^2Re\tilde{w}_Z. \tag{3.14}$$

3.4. *Linearized interface conditions*

The perturbed interface shown in figure 25 (Appendix A) is represented by $(x, h(x))$ in the Eulerian description. The material point P_0 present at $(X, Z=0)$ in the unstressed configuration is displaced to P in the base state, and is further displaced to P' upon introduction of perturbations. Importantly, the material point is still labelled by $(X, Z=0)$ within the Lagrangian description of the solid. In Appendix A, we show that the application of the velocity and stress conditions within the linear stability analysis does not require Taylor expansion of solid dynamical quantities in the vertical Lagrangian coordinate. The perturbed interface is in fact described by $X(x)$, $Z=0$ in the Lagrangian description of the solid. If an Eulerian framework is used (Chokshi 2007; Choskshi & Kumaran 2008), the expansion about $z=0$ is justified for the solid. Following the procedure discussed in Appendix A, the linearized interfacial conditions at the fluid–solid interface are

$$\tilde{v}_z = -\mathrm{i}kc\,\tilde{w}_Z, \tag{3.15}$$

$$\tilde{v}_x + 2\tilde{w}_Z = -\mathrm{i}kc\,\tilde{w}_X, \tag{3.16}$$

$$\boxed{-4\mathrm{i}k\Gamma\tilde{w}_Z + 2\frac{\mathrm{d}\tilde{w}_Z}{\mathrm{d}Z} - 2k^2c\eta_r\Gamma\tilde{w}_X}$$
$$+ \left(\frac{1}{\Gamma} - \mathrm{i}kc\eta_r\right)\left(\frac{\mathrm{d}\tilde{w}_X}{\mathrm{d}Z} + \mathrm{i}k\tilde{w}_Z\right) = (\mathrm{d}_z\tilde{v}_x + \mathrm{i}k\tilde{v}_z) - 2\tilde{w}_Z, \tag{3.17}$$

$$-\tilde{p}_s + 2\left(\frac{1}{\Gamma} - \mathrm{i}kc\eta_r\right)\frac{\mathrm{d}\tilde{w}_Z}{\mathrm{d}Z} - \boxed{4k^2c\eta_r\Gamma\tilde{w}_Z} = -\tilde{p} + 2\mathrm{d}_z\tilde{v}_z - \frac{\gamma}{\Gamma}k^2\tilde{w}_Z, \tag{3.18}$$

where $\gamma = \gamma^*/ER$ is the non-dimensional surface tension with γ^* being the dimensional fluid–solid interfacial tension. The term $2\tilde{w}_Z$ on the right-hand side of the tangential stress balance (3.17) arises due to the coupling between normal

displacement fluctuation and mean flow ($w'_Z \mathrm{d}_z^2 \overline{v}_x$), and this was absent in the analysis of Gkanis & Kumar (2005). This term is identically zero in plane Couette flow because of its linear velocity profile. Gkanis & Kumar (2005) also included an extra coupling term in normal stress balance ($w'_Z(\mathrm{d}\overline{p}_s/\mathrm{d}_Z)$) which is absent in the present analysis. These differences arise precisely due to the Taylor expansion of the (Lagrangian) solid quantities about $z=0$ in earlier works (Gkanis & Kumar 2005; Gaurav & Shankar 2009). Interestingly, these differences are absent in the case of plane Couette flow past a deformable solid (Gkanis & Kumar 2003), and they appear only in pressure-driven plane and pipe Poiseuille flows. We show later in this paper that the suggested modifications lead to some qualitative differences in the results at $Re=0$.

3.5. *Conditions at channel centreline*

When the thickness and moduli of the upper and lower linings are identical (in figure 1), there is a symmetry of the configuration about the channel centreline, since the base flow is also symmetric about the channel centreline $z=1$. The equations governing the fluid and solid are linear and homogeneous; consequently, the solution for $\tilde{v}_z$ can be separated into even and odd functions of $\tilde{v}_z$ about the channel centreline (Drazin & Howard 1966). The conditions at the centreline are different for the two modes, as follows.

(i) When $\tilde{v}_z$ is an odd function of z about the centreline, the value of $\tilde{v}_z$ and its second derivative $\mathrm{d}_z^2\tilde{v}_z$ are zero. Such modes are called 'varicose modes', which satisfy (at $z=1$):

$$\tilde{v}_z = 0, \;\; \mathrm{d}_z\tilde{v}_x = \frac{\mathrm{i}}{k}\mathrm{d}_z^2\tilde{v}_z = 0. \tag{3.19}$$

For such disturbances, the two fluid–solid interfaces oscillate out of phase with each other, thus giving rise to a varicose shape to the deformable channel walls with no crossflow at the centreline of the channel.

(ii) When $\tilde{v}_z$ is an even function of z, then its first and third derivatives are zero at the centreline. These modes are called 'sinuous modes', which satisfy (at $z=1$):

$$\tilde{v}_x = \frac{\mathrm{i}}{k}\mathrm{d}_z\tilde{v}_z = 0, \;\; \mathrm{d}_z^2\tilde{v}_x = \frac{\mathrm{i}}{k}\mathrm{d}_z^3\tilde{v}_z = 0. \tag{3.20}$$

For these disturbances, the two fluid–solid interfaces oscillate in phase with each other, and this gives rise to a sinuous shape to the deformable channel walls, with no axial flow at the centreline of the channel. It must be noted that there is some ambiguity in the literature on the nomenclature of these modes as 'symmetric' or 'antisymmetric', and this arises purely based on the choice of the variable upon which the nomenclature is based. For example, Drazin (2002) calls the sinuous modes 'antisymmetric' based on the axial perturbation velocities and streamlines. In contrast, Huerre & Rossi (1998) refer to the sinuous modes as 'symmetric' based on cross-stream perturbations. In this study, we simply refer to the modes as sinuous and varicose as discussed above, and use the respective conditions at $z=1$. Finally, the boundary conditions at rigid-bottom plate ($z=-H$) are

$$\tilde{w}_X = 0, \qquad \tilde{w}_Z = 0. \tag{3.21}$$

3.6. *Numerical methodology*

The linear stability of the composite fluid–solid system under consideration is determined by solving (3.9)–(3.21) for eigenvalue c, as a function of k, Re, Γ, H, η_r and γ. We employed a combination of asymptotic analysis (in the limit $Re \ll 1$)

and numerics to investigate the stability characteristics of the present configuration. A pseudospectral collocation method (Boyd 1989; Weideman & Reddy 2000) and a numerical shooting procedure with orthonormalization (Drazin & Reid 1981) were used to numerically evaluate the eigenvalues and neutral stability boundaries. In the numerical shooting procedure (Shankar & Kumaran 2000), a Runge–Kutta integrator was employed to determine the linearly independent solutions in the solid and liquid layers, and the interfacial conditions were used to set up a characteristic matrix, whose determinant was set to zero in order to determine the complex wave speed. A Newton–Raphson iterative technique was employed to solve the characteristic equation, which requires a good initial guess to converge to the desired eigenvalue. This is provided by the pseudospectral method, which gives the complete spectrum of eigenvalues c for specified values of other parameters. In the pseudospectral method, the unknown variables (e.g. velocity field in the fluid and displacement field in the solid) are expanded in a truncated series of N Chebyshev polynomials. These expansions are substituted in the linearized governing equations, and the resulting equations are set to zero on $N-8$ Gauss–Lobatto (Boyd 1989) collocation points. The remaining eight equations are generated from the boundary and linearized interface conditions. This yields a $N \times N$ matrix eigenvalue problem for N eigenvalues c, which are obtained using the 'polyeig' eigenvalue solver in Matlab. To filter out the spurious eigenmodes that may arise, the truncation level N is increased until the genuine modes are accurately identified. To further check the veracity of the eigenmodes, we provide these as an initial guess to the orthonormal shooting procedure discussed above, and it is ensured that the eigenvalue obtained from the spectral code is indeed genuine. These numerical results were validated by comparing the eigenvalues with (i) the analytical asymptotic results (described in Appendix B) obtained at low Re and low k, (ii) the results obtained for arbitrary k in the creeping-flow limit, where there are only two solutions to c which can be found exactly, and (iii) the results in the limit of a rigid channel, which can be recovered from our study by setting $\Gamma \to 0$. In all the comparisons, we found the agreement between the asymptotic predictions and the spectral and orthonormal shooting results.

4. Results and discussion

4.1. *Results in the zero-Re limit*

Gkanis & Kumar (2005) studied the linear stability of pressure-driven flow of a Newtonian fluid in a neo-Hookean deformable channel in the creeping-flow limit ($Re = 0$) by considering only varicose modes. They demonstrated that depending on solid thickness H and solid deformability parameter Γ, the flow could become unstable for finite- and/or high-wavenumber fluctuations. The finite-wavenumber instability is similar in nature to that in plane Couette flow (Gkanis & Kumar 2003). It was shown that for sufficiently thick solids ($H \gtrsim 10$), finite-wavenumber perturbations (with $k \sim O(0.1)$) become unstable first, while for $H \lesssim 10$, high-wavenumber perturbations (with $k > 3$) become unstable first. However, as we mentioned in § 3, their analysis did not include a term arising due to the coupling between the normal displacement fluctuation and mean flow ($w'_Z \mathrm{d}_z^2 \overline{v}_x$) in the tangential stress balance (3.17), but included an extra coupling term ($w'_Z(\mathrm{d}\overline{p}_s/\mathrm{d}_Z)$) in the normal stress balance (3.18). In order to determine the consequences of these differences, we first revisit the problem of stability of Poiseuille flow in a neo-Hookean deformable channel in the creeping-flow limit; the effect of inertia is analysed in detail in subsequent sections. In the $Re = 0$ limit, the characteristic equation is quadratic in

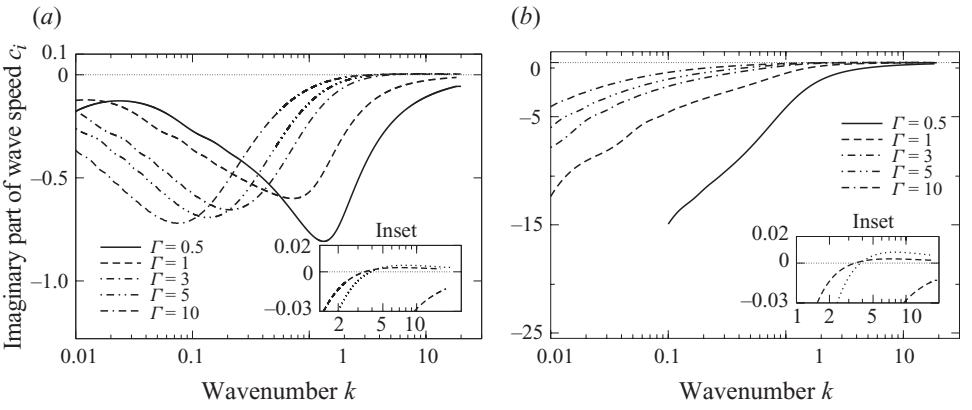

FIGURE 2. c_i versus k curves showing the absence of finite-k viscous mode instability in the creeping-flow limit for flow in a neo-Hookean deformable channel. Only the high-k instability is present for $k \gtrsim 3$ for both sinuous and varicose modes as Γ is increased. (a) Varicose modes: data for $H = 10$, $Re = 0$, $\gamma = 0$; (b) sinuous modes: data for $H = 10$, $Re = 0$, $\gamma = 0$.

wave speed c. One of the two roots for c becomes unstable at high wavenumbers when Γ is increased above a critical value, while the second root always remains highly damped for all values of k and Γ. Figure 2 depicts c_i versus k data for the first root and it shows that the short-wave perturbations ($k \gtrsim 3$) become unstable for higher values of Γ for both sinuous and varicose modes. This short-wave instability is essentially the instability driven by the first normal stress difference predicted by Gkanis & Kumar (2003, 2005) for different configurations. The stability characteristics of the normal-stress-driven short-wave fluctuations predicted here remain similar to the unstable short-wave mode described in Gkanis & Kumar (2005) for the present configuration and other different configurations. For example, the critical Γ remains independent of H and interfacial tension has a stabilizing effect on this instability driven by normal stress difference. Even the numerical data for critical values of Γ with the modified stress boundary conditions (used in the present study) changes very little as compared to the ones reported in Gkanis & Kumar (2005). It could further be expected that the instability for perturbations with wavelengths small compared to channel width would be independent of the nature of the symmetry of the modes (sinuous or varicose), as seen in figure 2.

However, an important feature to note in figure 2 is that the finite-wavenumber perturbations (with $k \sim O(1)$) do not become unstable for the values of Γ up to 10 for both sinuous and varicose modes. This is at variance with the earlier predictions (Gkanis & Kumar 2005) where it was shown that the Poiseuille flow in a neo-Hookean deformable channel becomes unstable at finite wavenumbers for sufficiently thick solids when Γ increases above a critical value. We attribute this difference to the modified stress continuity conditions implemented in this study, which are different from the ones used earlier (Gkanis & Kumar 2005). The results in figure 2 are shown for $H = 10$, but we have verified that the finite-k mode is always stable for any combination of H and Γ. Thus, the present study shows that the finite-wavenumber instability is absent for pressure-driven flow in a neo-Hookean deformable channel in the creeping-flow limit. A similar prediction was recently made for the case of pressure-driven flow in a deformable pipe (Gaurav & Shankar 2009). The unstable normal-stress-driven short-wave mode is the critical mode of instability for any value of solid thickness in the creeping-flow limit. It is also important to mention here

that the predictions for Couette flow past a neo-Hookean solid (Gkanis & Kumar 2003) will not be altered due to the modifications in boundary conditions suggested in this work. This is because both the coupling terms, $w'_Z \mathrm{d}^2_z \overline{v}_x$ (included in this work, and absent from the work of Gkanis & Kumar 2005) and $w'_Z(\mathrm{d}\overline{p}_s/\mathrm{d}_Z)$ (included in Gkanis & Kumar 2005, but removed in this work) in the tangential and normal stress balance, respectively, are identically zero for Couette flow due to its linear velocity profile.

4.2. *Results at low Reynolds number*

Owing to the modifications suggested for the interfacial stress conditions in this study, we find that there is no finite- or low-wavenumber instability in the creeping-flow limit in channel flow. But the limit of $Re \ll 1$ is not the same as $Re = 0$. Physically, this is because of the existence of shear waves in an elastic solid, which are a class of transversely propagating waves with wave speeds $\sim(E/\rho)^{1/2}$ (Achenbach 1973), and which exist only for finite inertia in the solid. These shear waves in an elastic solid can be destabilized by the fluid flow, and consequently, it is important to investigate the effect of inertia ($Re \neq 0$) on the stability of the system under consideration. The characteristic equation for $Re \neq 0$ admits multiple solutions to c unlike in the creeping-flow limit where the characteristic equation admits only two solutions to the wave speed. It is instructive to examine whether any of the roots of characteristic equation other than the ones corresponding to creeping-flow limit become unstable for $Re \neq 0$. To this end, we first discuss the results in the limit of small but finite Reynolds number and explore the intermediate and high-Re regime later. In our discussion below, we treat varicose and sinuous modes separately, as the qualitative nature of their instabilities is different.

4.2.1. *Varicose modes*

At $Re = 0$, we showed before that only the normal-stress-driven short-wave perturbations become unstable. This high-wavenumber instability continues to finite Reynolds number and the critical Γ required to destabilize the system remains an $O(1)$ quantity (as shown later in figure 9). Using the pseudospectral code which resolves the complete eigenspectrum, we explored different wavenumber regimes at low Reynolds number in order to investigate the possibility of unstable modes other than the unstable normal-stress-driven short-wave mode. Figure 3 shows the eigenvalue spectrum for $H = 5$, $Re = 0.1$ and $k = 0.1$ for different values of Γ. It shows that there are multiple solutions for the eigenvalue c, approximately half of which are downstream travelling waves (eigenvalues with positive real part c_r) and other half are upstream travelling waves (eigenvalues with negative real part c_r). The eigenspectrum in figure 3 shows that for lower values of $\Gamma = 0.4$ and 0.5, all the eigenmodes remain stable. As Γ is increased to 0.6, one of the upstream travelling modes becomes unstable. It must be noted here that modes are designated as 'upstream' or 'downstream' based on the sign of their phase speeds.

With further increase in Γ, more number of upstream travelling modes become unstable. It is also observed that the slowest upstream travelling wave (eigenvalue with smallest magnitude of real part) becomes unstable first as Γ is increased followed by the upstream modes with higher wave speeds. The slowest upstream travelling varicose mode is labelled 'Var-1u' and other upstream varicose modes are designated as 'Var-2u', 'Var-3u' etc., in increasing order of their wave speeds. Figure 3 also shows that none of the downstream travelling modes become unstable for any value of Γ.

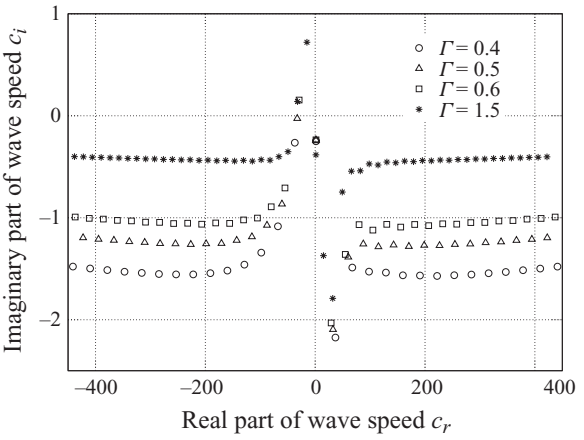

FIGURE 3. Eigenvalue spectrum illustrating instability of upstream varicose modes at low Reynolds number and low wavenumber: data for $H = 5$, $Re = 0.1$, $k = 0.1$, $\gamma = 0$ and $\eta_r = 0$.

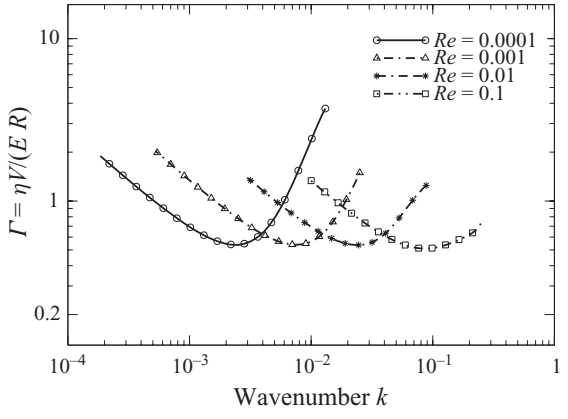

FIGURE 4. Varicose modes: neutral stability diagrams for unstable upstream mode at low Re and low k. Data for $H = 5$, $\eta_r = 0$ and $\gamma = 0$.

In fact, increasing Γ is found to have a stabilizing effect on downstream travelling waves.

Figure 4 shows the neutral stability curves in $\Gamma - k$ plane for the first upstream travelling varicose mode (Var-1u) for $H = 5$ at different values of Re. These neutral curves show that the flow becomes unstable for different bands of wavenumbers ranging from $O(0.001)$ to $O(0.1)$ depending on the value of Re. The neutral curves keep shifting towards the low-wavenumber regime with decrease in Reynolds number. The critical Γ (minimum of a given neutral curve) remains independent of Re while the critical wavenumber k_c decreases with decrease in Reynolds number. The critical conditions (Γ_{crit}, k_{crit} and c_r) corresponding to figure 4 are plotted in figure 5 as a function of Reynolds number. This figure illustrates that $\Gamma_{crit} \sim O(1), k_c \sim Re^{1/2}$ and wave speed $c_r \sim Re^{-1}$ in the limit of $Re \ll 1$. We have verified that the second upstream mode (Var-2u) also exhibits similar qualitative trends for $\Gamma - k$ neutral curves and show identical scalings as mentioned above. Recently, Gaurav & Shankar (2009) observed a very similar instability of upstream travelling modes at low Re and low k for Poiseuille flow in a neo-Hookean deformable tube. To elucidate the nature

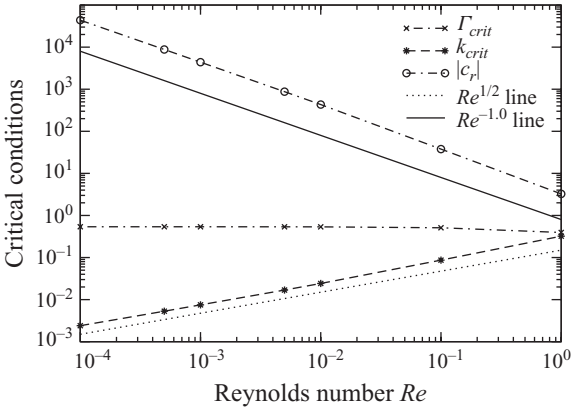

FIGURE 5. Varicose modes: scalings of Γ, k and c with Re for upstream low-Re instability. Data for $H = 5$, $\eta_r = 0$ and $\gamma = 0$.

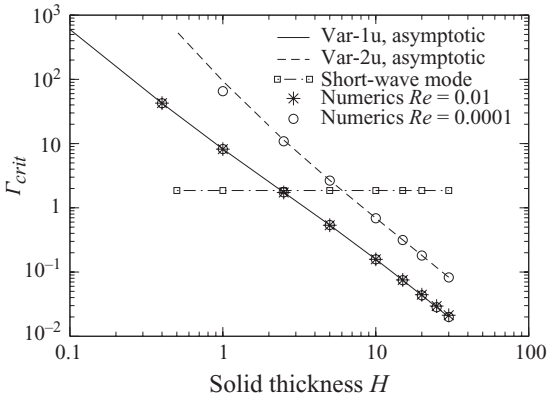

FIGURE 6. Varicose modes: variation of critical Γ with H for varicose modes (Var-1u, Var-2u) showing the agreement between asymptotic and numerical results. The critical Γ for the normal-stress-driven short-wave mode is also shown for comparison. Data for $\eta_r = 0$ and $\gamma = 0.05$ for the short-wave mode. The asymptotic and numerical results for Var-1u and Var-2u are independent of γ.

of these unstable modes at $Re \ll 1$ and $k \ll 1$, we sketch in Appendix B the outlines of an asymptotic analysis which predicts these modes. The analysis also helps clarify questions related to the existence of these unstable modes in other planar shear flows like the plane Couette flow past a deformable neo-Hookean solid. For example, it can be inferred from the asymptotic analysis that these low-k unstable modes cannot exist if one of the walls is rigid.

Figure 6 shows the variation of critical Γ with solid thickness H, obtained from asymptotic analysis as well as numerical solutions, for first two upstream modes. Both asymptotic and numerical predictions agree very well with each other. This figure shows that the critical Γ decreases progressively with increase in solid thickness. Figure 6 also compares the critical Γ for upstream travelling modes with the unstable short-wave mode in the limit of low Reynolds number. It shows that the Var-1u mode becomes unstable first for thick solids while the normal-stress-driven short-wave mode becomes unstable first for sufficiently thin solids ($H \lesssim O(1)$). While this conclusion holds only for varicose modes, it is possible that the critical Γ for sinuous

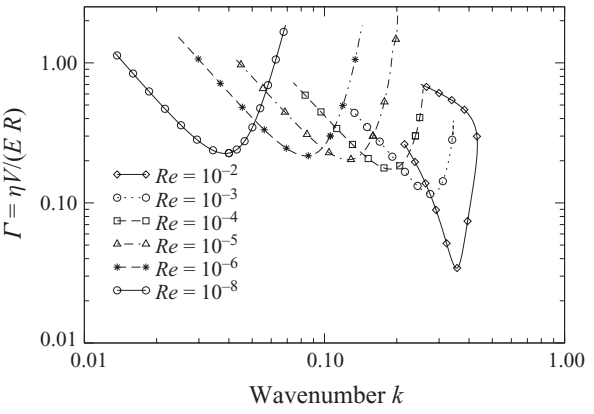

FIGURE 7. Sinuous modes: neutral curves in the Γ–k plane for $H = 5$ illustrating instability at low Re and low k; $\gamma = 0$, $\eta_r = 0$.

modes could be smaller than that for varicose modes, and this issue is addressed in the following subsection. Even though the critical Γ for short-wave mode are shown for $Re = 0.1$ and $\gamma = 0.05$ while the asymptotic results for upstream mode shown in figure 6 are valid for $Re \ll 1$, the comparison between the two modes can be made for $Re \ll 1$ because of the following reasons. The critical Γ for short-wave mode remains independent of Reynolds number for $Re < O(1)$ (see figure 9) and thus, the results for the normal-stress-driven short-wave mode for $Re = 0.1$ in figure 6 will also remain valid for $Re \ll 1$. Also, the low-k asymptotic analysis shows that the surface tension parameter does not affect the low-Re upstream modes and thus the results for upstream modes will be identical for both $\gamma = 0$ and $\gamma = 0.05$.

It is also appropriate here to comment on the divergence of c_r with Re in the limit of $Re \ll 1$. This divergent behaviour arises because the dimensional wave speed of the unstable fluctuations scale as the shear wave speed in the solid for $k \ll 1$: $c_r^* \propto (E/\rho)^{1/2} k^{-1}$. Since $k \propto Re^{-1/2}$, we obtain $c_r = c_r^*/V \propto Re^{-1}$. This divergence is a consequence of dividing a flow-independent wave speed with V, and since $V \to 0$ as $Re \to 0$ (with all other parameters fixed), we obtain a divergence of c_r with Re. However, to obtain the instability we also require $\Gamma = V\eta/(ER) \sim O(1)$ and for fixed values of R, ρ and η, if $Re \to 0$ this implies $V \to 0$, which means that E must also tend to zero in order to keep $\Gamma \sim O(1)$ constant. This implies that this class of unstable modes will be realized for $Re \ll 1$ only in the case of ultra soft solids. For solids with larger shear moduli, for $Re \ll 1$, these modes with $c_r \propto 1/Re$ remain stable. Thus, from a practical viewpoint the results in the $Re \ll 1$ limit are not very relevant. The utility of the $Re \ll 1$ limit is that it allows for analytical asymptotic solutions, which are used to ensure the accuracy and veracity of the numerical solutions. Further, the asymptotic analysis also allows us to develop some insight into the nature of the instability by showing that this instability is absent in (i) flows between one rigid wall and one deformable wall, and (ii) when the wall is modelled as a linear elastic solid. We also show below in § 4.4 that the presence of a small amount dissipation in the solid also removes the instability at $Re \ll 1$.

4.2.2. *Sinuous modes*

Using the spectral code, we identified a similar low-k instability for sinuous modes, but here the downstream waves are the most unstable modes. Figure 7 shows the neutral stability curves in the Γ–k plane for different Re. The instability extends to

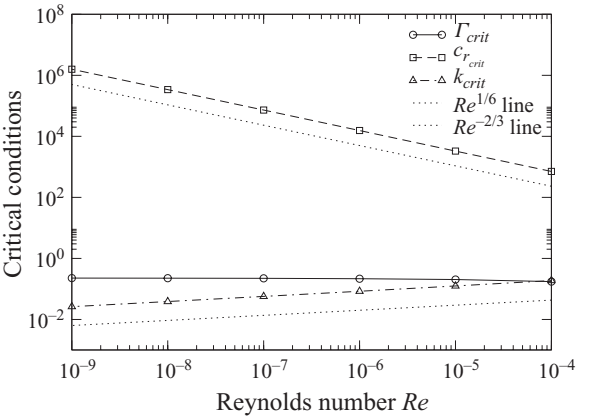

FIGURE 8. Sinuous modes: scalings of Γ_c, k_c and c_r with Re for upstream low-Re instability. Data for $H = 5$, $\eta_r = 0$ and $\gamma = 0$.

very low Re, and the critical value of Γ approaches an $O(1)$ constant as Re decreases. However, the critical k decreases as Re decreases. Figure 8 illustrates the scaling of Γ_c, k_c and c_r with Re for $Re \ll 1$. The sinuous modes show very different scaling behaviour compared to varicose modes, with $k_c \propto Re^{1/6}$ and $c_r \propto Re^{-2/3}$. We have not attempted an asymptotic analysis for this class of modes, but a preliminary scaling analysis suggests that these also belong to a class of shear waves in the solid wherein inertial effects in the solid are important. The inertial terms in the solid (3.13) are of $O(Rek^2c^2)$. With the scalings inferred from our numerical results, it can be easily verified that the inertial terms are of the same order as the elastic terms in the solid, even for $Re \ll 1$. A comparison of figures 4 and 7 show that sinuous modes are more unstable at least for $H = 5$. The issue of which mode (sinuous or varicose) becomes unstable first is addressed in detail in § 4.4.

4.3. *Unstable modes at high Reynolds number*

4.3.1. *Varicose modes*

It was demonstrated in previous section that for $Re \ll 1$, the low-k, upstream travelling waves (Var-1u, Var-2u, etc.) and the normal-stress-driven short-wave mode become unstable as the solid elasticity parameter Γ increases beyond a critical value. It is of interest to know whether these unstable modes in low-Re limit continue to intermediate and higher Reynolds number. Earlier studies on stability of fluid flow past a linear elastic deformable solid (Srivatsan & Kumaran 1997; Shankar & Kumaran 2001, 2002) have shown that there exists a set of multiple downstream travelling 'wall modes' which become unstable in the limit of high Reynolds number. These downstream wall modes continue to intermediate- and low-Reynolds-number limits within the linear elastic model for the deformable wall. However, it was shown in § 4.2 that the downstream travelling varicose modes do not become unstable in low-Re limit for Poiseuille flow in a neo-Hookean deformable channel. In this section, we explore different Reynolds number regimes to examine whether downstream travelling waves become unstable for pressure-driven flow in a neo-Hookean deformable channel.

We first focus our attention on the continuation of upstream travelling modes to high Reynolds number. Figure 9 shows the variation of critical Γ with Re for the first upstream mode (Var-1u) for two different values of solid thickness. There are, of course, other unstable upstream modes, but we have verified that they all

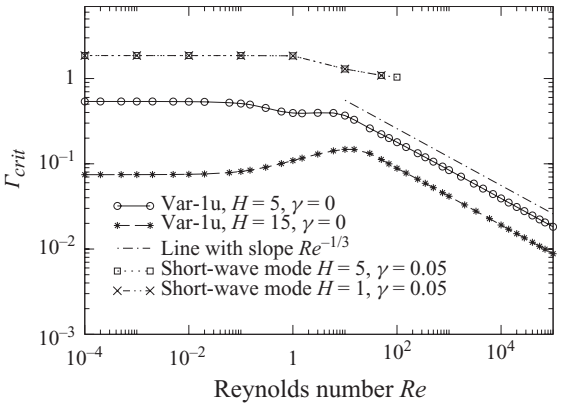

FIGURE 9. Varicose modes: continuation of first upstream mode to higher Reynolds number. Data for $\gamma = 0$ and $\eta_r = 0$.

show similar qualitative behaviour and thus the results are shown only for the first upstream travelling mode. We have further verified that Var-1u is the most unstable of the upstream travelling varicose modes at all Reynolds numbers. The figure shows that the critical Γ remains independent of Reynolds number for $Re \ll 1$, in agreement with low-Re asymptotic analysis (Appendix B). This upstream mode continues to intermediate and high-Re limit and Γ decreases as $Re^{-1/3}$ for $Re \gg 1$. The scaling behaviour of Γ with Re for these upstream modes is identical to the scaling shown by unstable downstream wall modes for Poiseuille flow in a linear elastic deformable tube (Shankar & Kumaran 2001). By plotting the eigenfunctions for these upstream modes for $Re \gg 1$, we inferred that the upstream modes indeed correspond to the class of wall modes described in Shankar & Kumaran (2001). In particular, there is a wall layer of thickness $O(Re^{-1/3})$ where viscous effects are confined near the fluid–solid interface (discussed below in figure 12). However, it must be mentioned here that the upstream travelling modes do not become unstable for flow past linear elastic solid for any Reynolds number. Figure 9 also shows that the effect of decreasing solid thickness is stabilizing for upstream travelling modes in both low- and high-Reynolds-number limits. Figure 9 also depicts the continuation of normal-stress-driven short-wave mode to intermediate Reynolds number. It illustrates that the critical Γ is independent of Reynolds number for $Re < O(1)$ and decreases slightly for $Re \sim O(100)$. As expected, the critical Γ for short-wave fluctuations does not vary with solid thickness, and the data for $H = 1$ and $H = 5$ lie on top of each other. We found it numerically difficult to continue the neutral curve for the short-wave mode beyond $Re \sim 100$.

Figure 10 shows the eigenspectrum for $H = 5$, $k = 0.8$ and $Re = 100$ for different values of Γ. The eigenvalue spectrum shows that for $\Gamma = 0.002$, all the eigenmodes remain stable. As Γ is increased to 0.01, one of the downstream travelling modes becomes unstable. With further increase in Γ to 0.03 or higher, other downstream travelling modes become unstable. When Γ is increased to sufficiently high values, both downstream and upstream travelling waves become unstable (unstable upstream modes are not shown in figure 10). It is also observed that the slowest downstream travelling wave (eigenvalue with smallest magnitude of real part of c) becomes unstable first with increase in Γ, followed by the downstream waves with next higher wave speeds. The downstream varicose modes are labelled as Var-1d, Var-2d, etc. in increasing order of their wave speeds, which is similar to the nomenclature adopted earlier for upstream travelling waves. These downstream travelling modes

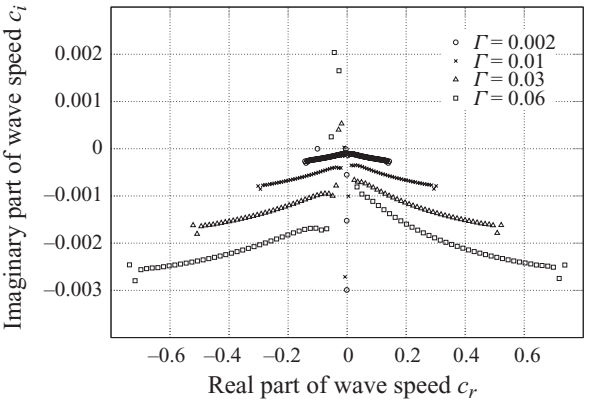

FIGURE 10. Varicose modes: eigenvalue spectrum for intermediate-Reynolds-number regime. Data for $H = 5$, $k = 0.8$, $Re = 100$, $\eta_r = 0$ and $\gamma = 0$.

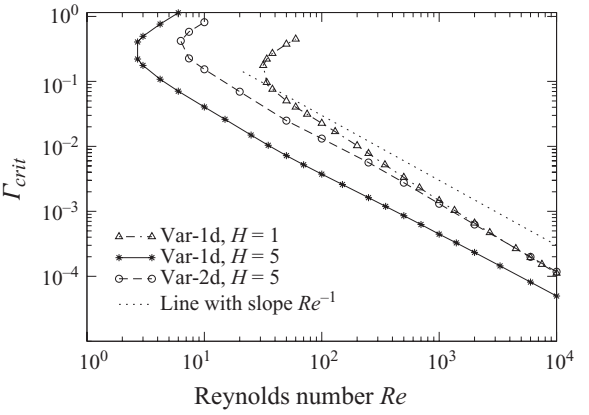

FIGURE 11. Varicose modes: variation of critical Γ with Re for downstream modes for two different values of solid thickness. Data for $\gamma = 0$ and $\eta_r = 0$.

were continued to both high and low Reynolds number. Figure 11 shows the variation of critical Γ with Re for the first two downstream modes for $H = 5$. It is observed that critical Γ decreases as Re^{-1} in the high-Reynolds-number limit. The scaling $\Gamma \sim Re^{-1}$ for $Re \gg 1$ suggests that these downstream modes correspond to the class of modes termed as 'inviscid modes' by Shankar & Kumaran (2000) for Hagen–Poiseuille flow in a linear elastic deformable tube. For these inviscid modes, the flow in the core is inviscid (but for the presence of a $O(Re^{-1/3})$ critical layer where the base flow velocity equals the wave speed c_r) and there is a wall layer of thickness $O(Re^{-1/2})$ smaller than the tube radius where the viscous effects are important. We have verified, by plotting the eigenfunctions and wall layer thickness as a function of Reynolds number that the downstream modes analysed in the present study indeed correspond to the class of inviscid modes described in Shankar & Kumaran (2000). In figure 12, we show the eigenfunctions for both wall modes and inviscid modes for varicose disturbances. For wall modes, the perturbation velocity is non-zero only near the fluid–solid boundary, while for inviscid modes, there is a sharp gradient near the fluid–solid boundary and also near the critical point, which is the point where the base flow velocity equals the wave speed for perturbations. The downstream travelling modes do not become

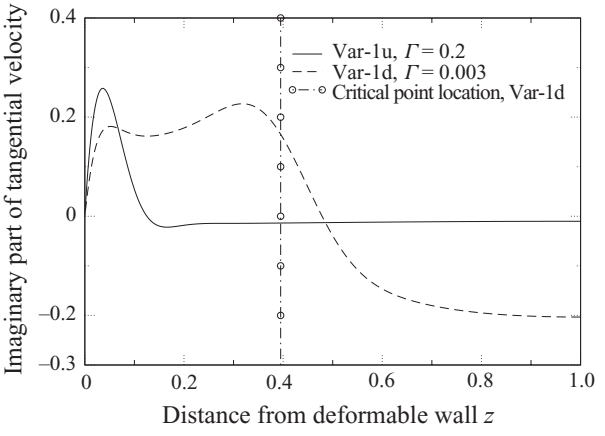

FIGURE 12. Eigenfunction plots for the two types of varicose modes predicted at higher Re: 'inviscid modes' and 'wall modes'. Data for $Re = 2000$, $k = 2$, $H = 1$, $\eta_r = 0$, $\gamma = 0$.

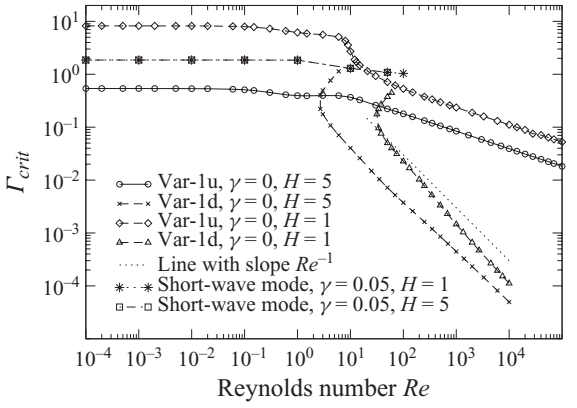

FIGURE 13. Comparison of critical Γ for different unstable modes in different regimes of Reynolds number. Data for $\gamma = 0$ and $\eta_r = 0$.

unstable in the low-Reynolds-number limit. For example, for $H = 5$ Var-1d remains stable below $Re \sim O(1)$. It is also observed that Var-1d is the most unstable of the downstream travelling varicose modes. Figure 11 also shows the variation of critical Γ with Re for Var-1d for a smaller value of solid thickness ($H = 1$). The effect of decreasing solid thickness is found to be stabilizing for downstream travelling waves.

Figure 13 compares the critical Γ for different unstable varicose modes (upstream, downstream and short-wave modes) for two different values of solid thickness. This figure shows that the Var-1d mode is most easily destabilized for $Re > O(10)$ for any value of solid thickness. However, for $Re < O(1)$, the critical mode of instability depends on thickness of the solid layer. For example, for $H = 5$, the Var-1u mode becomes unstable first while for $H = 1$, the normal-stress-driven short-wave mode becomes unstable first. Thus, in the limit of low Reynolds number (typically $Re \lesssim O(1)$), the first upstream mode (Var-1u) is the most unstable varicose mode for thick solids while the short-wave mode is most easily destabilized for sufficiently thin solids. Note that the data for short-wave mode is shown for non-zero interfacial tension ($\gamma = 0.05$) while the data for upstream and downstream modes is shown for $\gamma = 0$. We have verified that the interfacial tension has little stabilizing effect on upstream

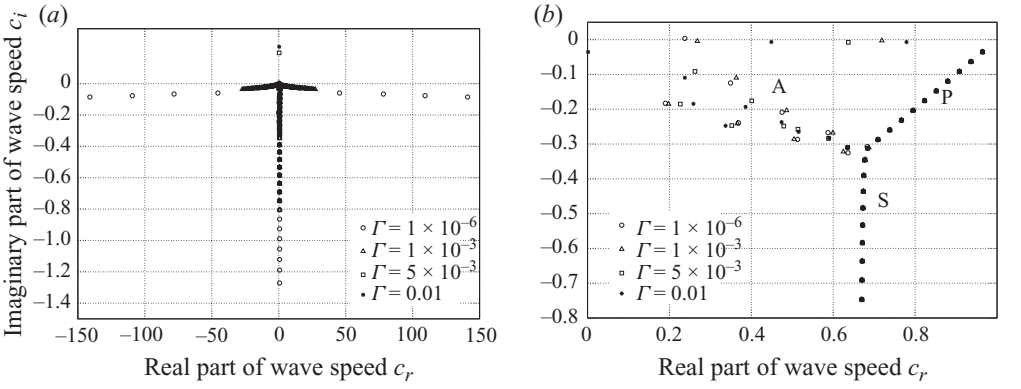

FIGURE 14. Eigenvalue spectrum for sinuous modes as a function of Γ showing the effect of wall deformability. (*a*) Full eigenvalue spectrum. (*b*) Enlarged portion of the spectrum where the eigenmodes for a rigid channel are usually located, illustrating the effect of wall deformability on the A, P and S types of modes in a rigid channel. Data for $H = 1$, $Re = 10\,000$, $k = 1$ and $\gamma = 0$.

and downstream travelling waves and critical Γ does not change significantly with increase in surface tension for upstream or downstream modes.

4.3.2. *Sinuous modes: effect of wall deformability on the Tollmien–Schlichting instability in a channel*

In this section, we discuss the instability of sinuous modes in a deformable channel at higher Reynolds numbers of $O(1000)$ and its relation to the TS instability in a rigid channel and the low-Re, low-k instability of sinuous modes discussed earlier in § 4.2. We first examine the effect of wall deformability on the TS instability in a rigid channel, which is also a sinuous mode. The limit of a rigid channel is obtained by taking $\Gamma \to 0$ first, and letting Re be arbitrary. Upon increasing Γ for a fixed non-zero H, the channel walls become more deformable. We first illustrate in figure 14 how the eigenvalue spectrum changes due to increase in wall deformability. In rigid-walled channels (Schmid & Henningson 2001) it is well known that the eigenvalues are located on three main branches labelled as A ($c_r \to 0$), P ($c_r \to 1$) and S ($c_r \approx 2/3$). The eigenmodes in the A branch correspond to wall modes, and the modes in the P branch correspond to centre modes. In the case of a deformable channel, even when Γ is very low ($\sim 10^{-6}$ in figure 14*a*, corresponding to a nearly rigid channel), there will be a set of travelling waves with positive and negative phase speeds, which remain stable. The usual Y-shaped spectrum of the truly rigid channel is evident upon enlarging the region (figure 14*b*) where the rigid-wall spectrum is normally located, and this part of the spectrum agrees very well with the spectrum for rigid-walled channels reported in Schmid & Henningson (2001). Upon increase in Γ to 10^{-3} and further to 10^{-2}, we find that only the A-type modes are affected, while the other two types of modes (P and S) remain unaffected. Apart from this effect of deformability on modes that already exist in a rigid-walled channel, modes that exist only in a deformable wall also become unstable upon increase in Γ.

In order to illustrate the effect of wall deformability on the TS mode, we plot the neutral curves in the Re–k plane. Figure 15 shows the effect of wall deformability on the TS mode for two different values of $H = 1$ and $H = 5$. For $H = 5$ (*a*), when $\Gamma \to 0$, the TS neutral curve in a rigid channel is recovered from our numerical results. Upon increase in Γ, the critical Re for the TS mode increases and the area of the unstable

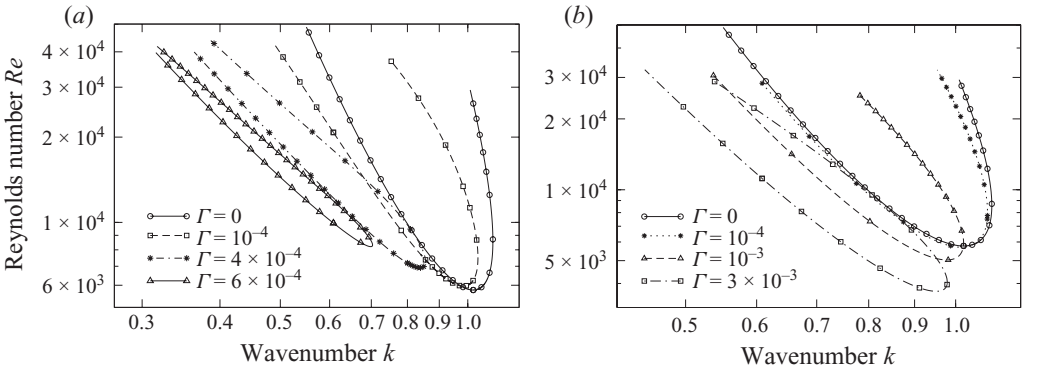

FIGURE 15. Sinuous modes: effect of wall deformability on the TS instability for two different wall thicknesses. Deformability has a destabilizing effect on the TS instability for $H = 1$ (b), while it has a stabilizing effect for $H = 5$ (a).

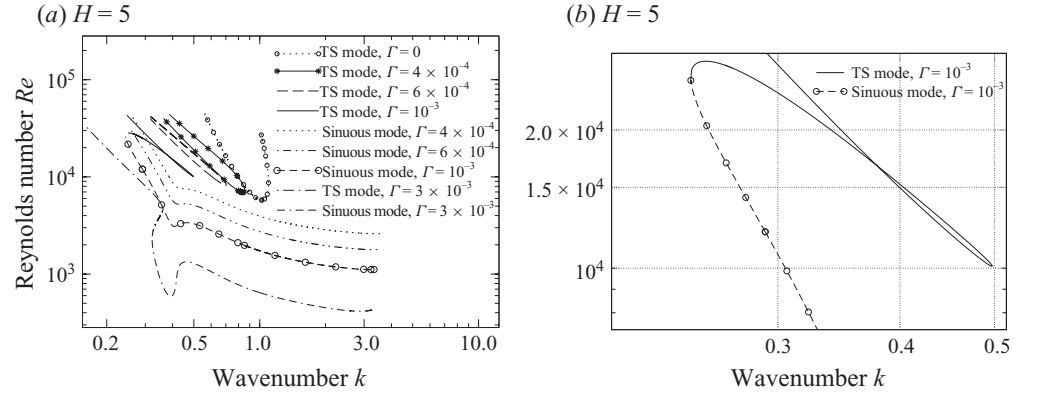

FIGURE 16. Sinuous modes: with increase in wall deformability, the TS mode 'coalesces' with a wall-induced instability, to give rise to a single unstable mode that continues to low Re.

region shrinks, thus indicating that the TS mode is stabilized by wall deformability. This prediction is in general agreement with many earlier studies reviewed in § 2. However, for $H = 1$ (figure 15b), the critical Reynolds number decreases with increase in Γ without a significant decrease of the area of the unstable region, thus showing a destabilizing effect of wall deformability. To our knowledge, a destabilizing effect of wall deformability on the TS mode in a channel flow has not been predicted before. However, most of the earlier studies on channel flow (Hains & Price 1962; Davies & Carpenter 1997; LaRose & Grotberg 1997) have used a simple spring-backed membrane model for wall deformability, and it is likely that such a simplistic model for wall is not sufficient to capture the destabilizing effect.

Earlier works (Davies & Carpenter 1997) on channel flow have also predicted the coalescence of the TS instability with another instability which is induced by wall deformability for deformable walls modelled as spring-backed membranes. In figures 16 and 17, we present results which show very similar behaviour even in deformable walls modelled as a neo-Hookean solid, both for $H = 5$ and $H = 1$. Let us first discuss the $H = 5$ case in figure 16(a). At small but non-zero values of Γ (upto $\Gamma = 6 \times 10^{-4}$), the TS mode remains distinct as in figure 15. In addition, there is another mode (termed 'sinuous mode' in figure 16a) which is unstable at $Re \sim 2000$

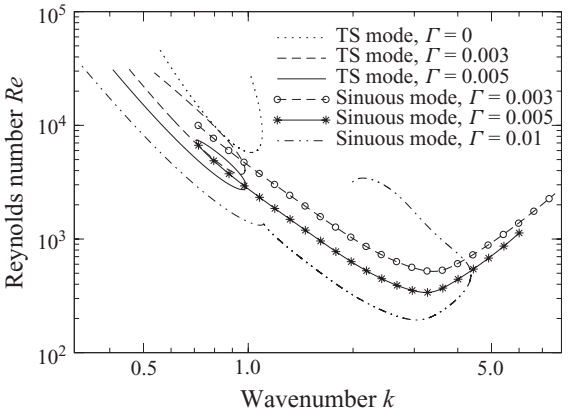

FIGURE 17. Sinuous modes: demonstration of mode coalescence of the TS mode with a wall-induced instability for $H = 1$.

for $\Gamma = 6 \times 10^{-4}$. Thus, while the TS mode is stabilized for this value of Γ, wall deformability has induced another more powerful unstable mode which becomes unstable at a much smaller Re compared to the critical Re of the TS mode in a rigid channel. Upon further increase in Γ to 10^{-3}, the two neutral curves merge into one single curve, and with further increase in Γ to 3×10^{-3}, the critical Re for this unstable mode is about 600. This clearly demonstrates a sort of 'mode coalescence' between the TS mode and the other unstable mode induced by wall deformability. Further, it could be concluded that with a single-layer neo-Hookean solid, it is not possible to delay the TS instability because of the presence of a more powerful unstable mode induced by wall deformability.

In a manner very similar to the above discussion, figure 17 demonstrates the mode coalescence of the TS mode with a wall-deformability-induced instability (termed 'sinuous mode') for $H = 1$. The main difference between figures 16(a) and 17 is that for $H = 5$ wall deformability (i.e. increase in Γ) stabilizes the TS mode, but for $H = 1$, wall deformability has a destabilizing effect. Regardless of the effect of deformability on the TS mode, there exists another more unstable mode at non-zero Γ which is induced by wall deformability, and the TS mode coalesces with this mode for both $H = 5$ and $H = 1$ to give rise to a single and more powerful instability with $Re_c \sim O(200)$ for $\Gamma \sim 0.01$. Thus, the phenomenon of mode coalescence makes the issue of stabilization of TS instability somewhat irrelevant, as the coalesced mode is highly unstable upon increase in wall deformability, as illustrated subsequently in figure 20.

Figure 18 illustrates the mode coalescence phenomenon in detail in the c_i–k plane for $H = 1$. When $\Gamma \to 0$, the only possible instability is the TS instability in a rigid channel, and this is shown in terms of c_i (proportional to growth rate) as a function of k. This curve shows that for a small band of wavenumbers $k \sim 1$, the flow is unstable ($c_i > 0$). For $k \ll 1$, and $k \gg 1$, the flow is stable. When Γ is increased to 0.003, the TS mode is destabilized (with c_i values greater than those for $\Gamma = 0$, though at smaller wavenumbers), but for $k \ll 1$ and $k \gg 1$, the curve for $\Gamma = 0.003$ approaches that of $\Gamma = 0$. There is another instability due to wall deformability ('sinuous mode'), which has much larger values of c_i, and has distinctly different behaviour for $k \ll 1$ and $k \gg 1$. When Γ is increased further to 0.005, we find that the two modes 'mix' at some intermediate value of k. Beyond a critical Γ, while for $k \ll 1$ a given mode

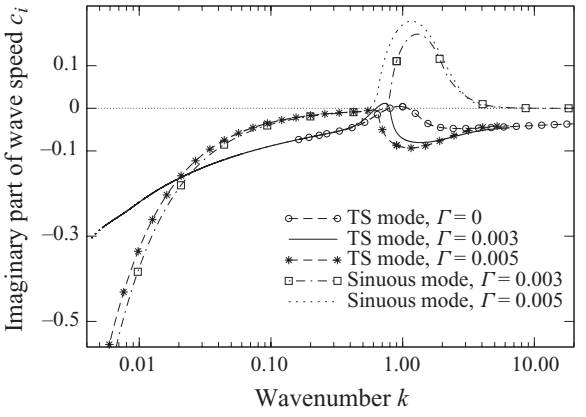

FIGURE 18. Illustration of coalescence of the TS mode with a wall-induced instability for $H = 1$ through c_i versus k curves for both the modes. $Re = 10\,000$, $\eta_r = 0$.

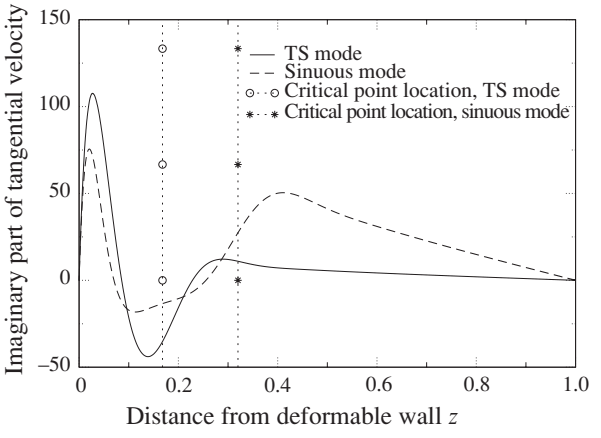

FIGURE 19. Eigenfunction plots for the TS mode and the other wall-deformability-induced sinuous mode. Data for $Re = 6000$, $k = 0.9$, $H = 1$, $\Gamma = 0.003$, $\eta_r = 0$, $\gamma = 0$.

will approach the low-k behaviour characteristic of that mode, but for $k \gg 1$, it will approach the high-k behaviour of the other mode. Thus labelling a given mode as 'TS' or 'sinuous' is arbitrary after the modes have coalesced, since the labelling will not be applicable in some regime of wavenumbers. Interestingly, similar mode-mixing behaviour has previously been observed for free-surface flow past a deformable layer by Gaurav & Shankar (2007), and in two-layer viscoelastic flows by Shankar (2004).

Figure 19 shows the eigenfunctions for the TS mode and the unstable mode induced only by wall deformability for the same set of parameters. The only difference between the two modes is their real part of the wave speed c_r. Both the modes show a wall layer close to fluid–solid interface, and presence of variations in perturbation velocity near the critical point (where $U = c_r$) is more prominent in the TS mode compared to the sinuous mode.

Figure 20 shows that the neutral modes in figure 16(a) continue to very low Re upon increase in wall deformability Γ, and eventually merge with the low-k instability discussed in § 4.2 for sinuous modes. These modes show a scaling of $Re \propto k^6$ or $k \propto Re^{1/6}$ for $Re \ll 1$ and $k \ll 1$. Another issue of interest is the effect of dissipative

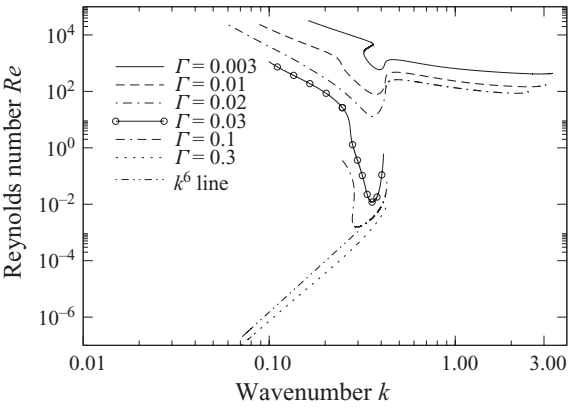

FIGURE 20. Sinuous modes: after mode coalescence, with increase in wall deformability, the instability continues to much lower Re for $H = 5$, $\eta_r = 0$.

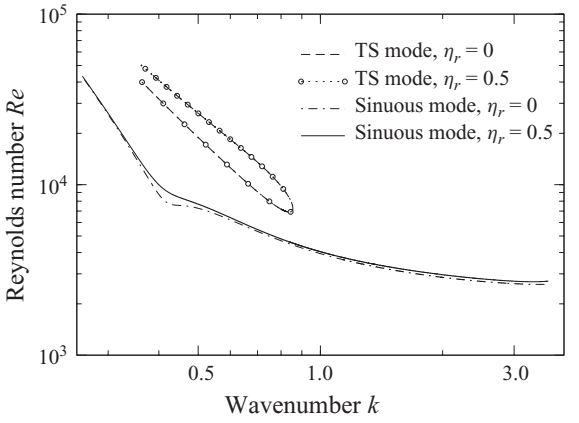

FIGURE 21. Effect of η_r on the instability due to sinuous modes at higher Reynolds numbers. Data for $H = 5$.

stresses in the solid on the instability. Previous studies (Yeo 1988; Davies & Carpenter 1997) have shown that dissipation has a slight destabilizing effect on the TS mode, but has generally has a stabilizing role on the instability, except in the case of static divergence which is destabilized by dissipation in the wall. Figure 21 shows that, even with the neo-Hookean model, we find that dissipation in the wall ($\eta_r \neq 0$) has a very small destabilizing effect on the TS mode, and has a mild stabilizing effect on the sinuous mode.

4.4. *Comparison of varicose and sinuous modes*

While the previous discussion has focused on the nature of the instabilities in specific regimes for varicose and sinuous modes separately, it is useful from the practical/experimental viewpoint to combine all the results in a single plot which yields the critical Reynolds number (Re_c) as a function of the wall elasticity parameter $\Sigma = \rho E R^2/\eta^2$. Figure 22 shows the neutral curves for all the modes in the Re-Σ plane for $H = 5$. It must be noted that Σ can be calculated by fixing the channel width, fluid density and viscosity and wall shear modulus E. For a value of Σ thus calculated for a given fluid–solid system, figure 22 shows the critical Re required for the instability.

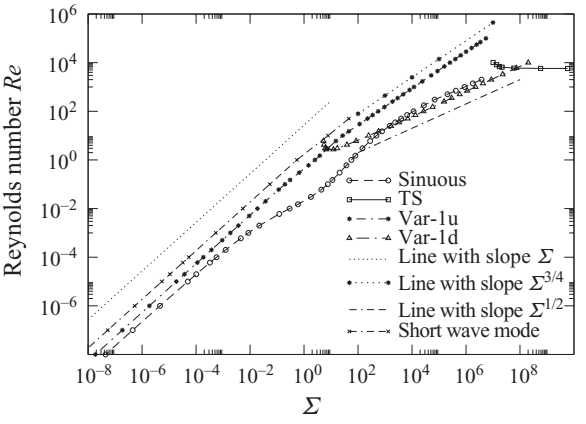

FIGURE 22. Comparison of sinuous, varicose and short-wave instabilities for $H = 5$, $\eta_r = 0$. Variation of critical Reynolds number Re_c with the solid elasticity parameter Σ.

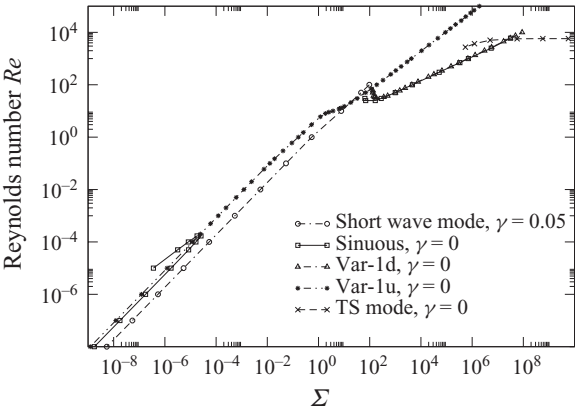

FIGURE 23. Comparison of sinuous, varicose and short-wave instability neutral curves for $H = 1$, $\eta_r = 0$: variation of critical Reynolds number Re_c with solid elasticity parameter Σ.

The limit of $\Sigma \to \infty$ represents a rigid channel, and $Re_c = 5771$ for the TS mode in a rigid channel. In a deformable channel, this mode continues to finite but large values of $\Sigma \sim 10^8$ as shown in the figure. However, the TS mode coalesces with a sinuous mode as Σ is decreased further, and this is shown in this figure by merely plotting the corresponding two neutral curves. The most unstable mode for $\Sigma \approx 10^4$–10^8 is the downstream varicose mode, which was identified as an 'inviscid mode' in § 4.3. For $\Sigma > 10^8$, the TS mode is the most unstable mode with $Re_c \sim 5771$. For $\Sigma < 10^3$, the continuation of the sinuous mode (which coalesced with the TS mode) is the most unstable mode. The short-wave instability is never critical for any value of Σ for $H = 5$. For small values of Σ, Re_c scales as $Re_c \propto \Sigma$, while for Σ in the range 10^4–10^8, $Re_c \propto \Sigma^{1/2}$, and for $\Sigma > 10^8$ $Re_c \to 5771$. The key feature that emerges from this figure is that modes of different symmetry are critical at different regimes of Σ, and hence it is important to consider both sinuous and varicose modes in order to accurately predict instabilities in a deformable channel.

Figure 23 compares both the sinuous and varicose modes along with the short-wave instability for $H = 1$. This shows that for smaller values of $\Sigma < 100$, the

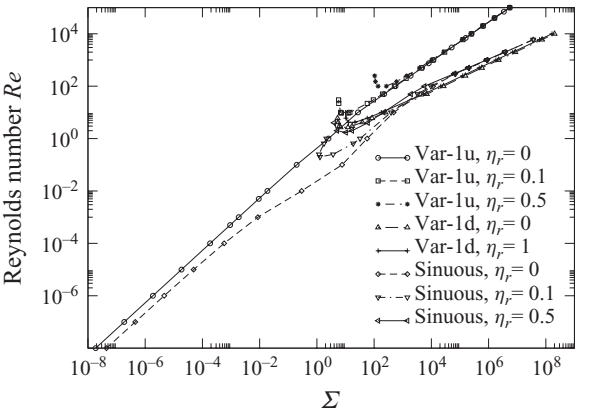

FIGURE 24. Effect of η_r on sinuous and varicose modes for $H = 5$: variation of critical Reynolds number Re_c with solid elasticity parameter Σ.

normal-stress-driven short-wave instability is most critical, while both the downstream sinuous and varicose modes are the most critical for $\Sigma > 10^4$. For $\Sigma > 10^7$, the continuation of the TS instability is the most critical mode. The effect of dissipation in the solid is analysed for both sinuous and varicose modes in figure 24. In general, the instabilities at low Σ (hence, also low Re) are removed by dissipative stresses in the solid. For example, by increasing η_r from 0 to 0.1, the instability sets in only after a $\Sigma \sim 100$ for varicose modes, but it sets in at $\Sigma \sim 1$ for sinuous modes. At higher $\Sigma > 1000$, the presence of non-zero η_r has negligible effect on the neutral curves. Dissipative effects tend to have a more severe stabilizing effect on varicose modes compared to sinuous modes.

Our numerical results show that when the solid elasticity parameter Σ is greater than a threshold value Σ_{max}, then $Re_c \to 5771$, the value corresponding to the TS instability in a rigid channel. From an experimental standpoint, it is useful to ask when will the critical Reynolds number for flow in a deformable channel be smaller than 5771. In order for the instabilities induced by the wall deformability to be present, it is necessary to have the parameters that determine Σ, i.e. elastic modulus, fluid viscosity, channel half-width and fluid density such that $\Sigma < \Sigma_{max}$. For $H = 5$, our numerical results show that $\Sigma_{max} \approx 10^8$, and if we choose water as the liquid with $\eta = 10^{-3}$ Pa s, $\rho = 10^3$ kg m^{-3}, and channel half-width as 10^{-3} m, we estimate the shear modulus E of the deformable wall to be $\leqslant 10^5$ Pa. Instead of water, if we choose air as the fluid ($\rho = 1$ kg m^{-3}, $\eta \approx 10^{-5}$ Pa s), and the channel half-width to be 10^{-2} m, then the shear modulus E must be smaller than 100 Pa for the instabilities to be induced by wall deformability. This would correspond to an extremely soft solid, which is unlikely to be of practical importance. Thus, the instabilities predicted in this work would be relevant for deformable channels with half-width of $O(1$ mm) and smaller, and for viscous liquids (with viscosities equal to or greater than that of water). Only for such systems Re_c will be significantly lower than 5771, and the shear modulus of the wall to realize these new instabilities is in the realistic range of $E \sim O(10^5)$ Pa and larger.

While it would be desirable to compare our predictions with experiments, we are not aware of systematic experimental studies documenting the onset of instability in (rectangular) deformable channels. The work of Shrivastava *et al.* (2008) addressed

this issue in an indirect manner by showing enhancement of mass transfer in a channel with a single deformable wall. In the low-Re limit, for plane Couette flow between a rigid wall and a deformable wall, experiments of Kumaran & Muralikrishnan (2000) and Eggert & Kumar (2004) predict an instability which confirms the theoretical predictions of Kumaran, Fredrickson & Pincus (1994) and Gkanis & Kumar (2003). In the higher-Re regime, the majority of experimental and theoretical studies in the area of flow past deformable walls has been devoted to boundary-layer flows. Even in that context, there is no consensus (Gad-el-Hak 2003) on whether the TS mode can be suppressed completely without making other modes unstable in boundary-layer flow past a deformable wall. Within the parameter regimes explored, our study shows that it is not possible to raise critical Re of the flow above the rigid-wall value of 5771 because of the destabilization of other (deformability-induced) modes in the system.

5. Conclusions

Using a nonlinear neo-Hookean model for the solid walls, we have analysed the stability of pressure-driven flow in a deformable channel for a wide variety of parametric regimes, considering both sinuous and varicose perturbations. The present study shows the importance of considering perturbations with both the symmetries, as either of them could become the critical mode depending on the parametric regime. In the creeping-flow limit, we predict the existence of only the short-wave instability, and the finite-wavelength instability is absent. At low (but non-zero) Re, we find that a class of shear waves in the solid are destabilized by the flow for both sinuous and varicose perturbations. These unstable modes continue to intermediate and high Re. At high Re, for sinuous modes, we find that the TS instability in a rigid channel coalesces with another instability induced by wall deformability, and this mode continues to very low Re as the wall becomes highly deformable. Thus, using only a single neo-Hookean solid layer, it is not possible to stabilize the TS mode in a channel flow without introducing additional unstable modes. In addition, at high Re, we find generally two class of unstable modes that are destabilized by solid deformability, i.e. the inviscid modes for which $Re_c \propto \Sigma^{1/2}$ and wall modes for which $Re_c \propto \Sigma^{3/4}$. In all the regimes considered, the wall modes are not relevant, and the inviscid modes are the most critical for $10^4 < \Sigma < 10^8$. For $\Sigma > 10^8$ the continuation of the TS mode in the rigid channel is the most unstable mode.

Finally, we provide some dimensional estimates of parameters for which the instabilities predicted here can be realized in experiments. Assuming $H = 5$, $E = 10^3$ Pa, $R = 100\,\mu$m, $\rho = 10^3\,\mathrm{kg\,m^{-3}}$, $\eta = 10^{-3}\,\mathrm{Pa\,s}$, we obtain $\Sigma = \rho E R^2/\eta^2 \sim 10^4$. From figure 22, the corresponding value of $Re_c \sim 10$, from which the velocity of the flow in the channel must be at least 10 $\mathrm{cm\,s^{-1}}$. For $R = 1$ μm, while keeping E, η and ρ the same as above, we obtain $\Sigma = 1$, for which $Re_c \sim 10^{-2}$ from figure 22. For this Re_c, the dimensional velocity is 1 $\mathrm{cm\,s^{-1}}$. Both the estimated values of velocities are typical of microfluidic applications (Thomas *et al.* 2010; Verma *et al.* 2008). Thus, the instabilities predicted here could be realized and potentially exploited in deformable channels encountered in microfluidic applications, but are not likely to be relevant in applications with channel widths of $O(1$ cm) or larger.

Acknowledgement is made to the Department of Science and Technology, New Delhi, India, for partial support of this research through an Intensification of Research in High Priority Areas (IRPHA) grant.

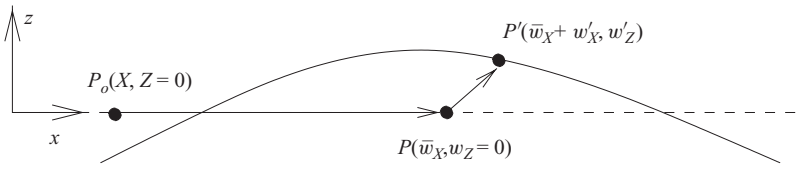

FIGURE 25. Schematic diagram illustrating the application of boundary conditions over the perturbed fluid–solid interface.

Appendix A. Linearization of continuity conditions at the fluid–solid interface

In this appendix, we provide the details of the linearization of the interfacial continuity conditions at the fluid–solid interface leading to the linearized conditions (3.15)–(3.18) in the main text of the paper. In this work, an Eulerian framework is used to describe the fluid dynamics, while a Lagrangian approach is used for the deformation in the solid. The basis underlying the derivation is the fact that a material particle's Lagrangian label remains unchanged upon introduction of perturbations to the fluid–solid interface. If a material point on the unperturbed interface (figure 25) is located at $(X, Z=0)$ in the unstressed configuration, its label remains the same even in the perturbed interface. As shown in figure 25, a material particle P_0 with Lagrangian label $(X, Z=0)$ in the unstressed state is displaced to point P $(\overline{w}_X, 0)$ in the deformed base state. Upon introduction of perturbations to the interface, the point P moves to P' $(\overline{w}_X + w'_X, w'_Z)$, where w'_X and w'_Z are the Lagrangian displacements of the material particle P from the deformed base state of the solid. The conditions at the perturbed fluid–solid interface $(X, Z=0)$ are continuity of velocities and stresses. Denoting F and S to be the fluid and solid dynamical quantities, respectively, the continuity conditions at the perturbed interface can be schematically written as

$$F(x, z, t)|_{P'} = S(X, Z, t)|_{P'}. \tag{A 1}$$

The current position of the point P' is unknown *a priori* and since Eulerian coordinates are used for liquid layers, any fluid dynamical quantity on the left-hand side of (A 1) is expressed by Taylor expansion about the known position of the unperturbed flat interface $(z=0)$. Thus, the left-hand side of (A 1) is given as

$$F(x, z, t)|_{P'} = F|_{P(z=0)} + h(x)\left(\frac{\partial F}{\partial z}\right)_{P(z=0)}, \tag{A 2}$$

where $h(x) = w'_Z(X, Z=0)$ is the vertical displacement of the material particle P_0 at its current position P. The current coordinates of the material particle P_0 at the point P' can also be expressed in terms of the displacements as $x = \overline{w}_X(X, Z=0) + w'_X(X, Z=0)$. Defining the displacement in the base state about the unstressed state as $\overline{u}_X(Z) \equiv \Gamma[H^2 - Z^2] + 2\Gamma(Z+H)$ (see (3.7)), the x-coordinate of material point P_0 can be written as $x = X + \overline{u}_X(Z=0) + w'_X(X, Z=0)$. For a specified current position x, the Lagrangian coordinate of the material point P_0 is obtained from the fundamental definition $X = x - \overline{u}_X(Z=0) - w'_X(X, Z=0)$. When the solid dynamical quantities are evaluated at this Lagrangian coordinate, this would be tantamount to evaluating the quantities at the perturbed interface. Therefore, the right-hand side of (A 1) is simply given as

$$S(X(x), Z, t)|_{P'} = S(X = x - \overline{u}_X(Z=0) - w'_X(X, Z=0), Z=0, t). \tag{A 3}$$

In other words, a Taylor expansion (in the vertical Lagrangian coordinate) about the unperturbed interface for the solid is not required, as the perturbed interface is in fact

described by $X(x), Z=0$ in the Lagrangian description of the solid. If an Eulerian framework is used (Chokshi 2007; Choskshi & Kumaran 2008), the expansion about $z=0$ is justified for the solid.

Following the above procedure, the continuity of normal velocity at perturbed fluid–solid interface is given exactly by

$$v_z(x,z)|_{P'} = \left(\frac{\partial w_Z}{\partial t}\right)_{X=x-\overline{u}_X(Z=0)-w'_X(X,Z=0),Z=0}. \tag{A 4}$$

Using Taylor expansion to express the left-hand side of (A 4) and retaining the terms that are linear in perturbation quantities, (A 4) can be written as

$$v'_z(x,z=0) = \left(\frac{\partial w'_Z}{\partial t}\right)_{X=x-\overline{u}_X(Z=0)-w'_X(X,Z=0),Z=0}. \tag{A 5}$$

Expressing the perturbation variables in terms of Fourier modes, i.e. on substituting $v'_z(x,z=0)=\tilde{v}_z(z=0)\exp[\mathrm{i}k(x-ct)]$ and $w'_Z=\tilde{w}_Z(Z=0)\exp[\mathrm{i}k(X-ct)]$ and rearranging, we obtain

$$\tilde{v}_z(z=0)\mathscr{E} = -\mathrm{i}kc\tilde{w}_Z(Z=0), \tag{A 6}$$

where $\mathscr{E}\equiv\exp[\mathrm{i}k(\overline{u}_X(Z=0)+w'_X(X,Z=0))]$. The remaining three interfacial conditions (tangential velocity and the normal and tangential stress continuity conditions) can be similarly derived and the factor $\mathscr{E}$ multiplies all the fluid perturbation variables in each of the three remaining conditions. For example, the linearized tangential velocity balance is

$$\tilde{v}_x(z=0)\mathscr{E} + \tilde{w}_Z(Z=0)\mathrm{d}_z\overline{v}_x|_{z=0} = -\mathrm{i}kc\tilde{w}_X(Z=0). \tag{A 7}$$

The factor $\mathscr{E}$ multiplies fluid perturbation variables in all the four interfacial conditions, and hence must be linearized within a linear stability analysis. This can be achieved by noting that $w'_X \ll \overline{u}_X$, thus yielding within a linear analysis $\mathscr{E}\approx\mathscr{E}_1=\exp[\mathrm{i}k(\overline{u}_X(Z=0)]$. The base-state displacement $\overline{u}_X(Z=0)$ of the wall at the unperturbed interface is independent of X, and hence is a constant for a fixed value of Γ (see (3.7)). All the four interfacial conditions have $\mathscr{E}_1$ multiplying the fluid quantities, and the differential equations governing the fluid (defined in (3.9)–(3.11)) are linear and homogeneous. The perturbation fluid velocities and pressure in the governing equations can then be multiplied by the quantity $\mathscr{E}_1$, and that will leave the Orr–Sommerfeld equation for the fluid invariant. Thus, the presence of a constant scaling factor $\mathscr{E}_1$ multiplying the fluid dynamical quantities in the linearized interface conditions does not alter the eigenvalue c. Following the procedure described above, we obtain the linearized conditions at the interface given in (3.15)–(3.18) of the main text, where the factor $\mathscr{E}_1$ is omitted without loss of generality because the governing Orr–Sommerfeld equation is linear and homogeneous.

Appendix B. Asymptotic analysis of varicose modes in the low-Re and low-k limit

In this appendix, we briefly sketch the asymptotic analysis used to compute the unstable varicose modes at low Re and low k. The analysis is similar to the one employed earlier for tube flow (Gaurav & Shankar 2009). Based on the discussion in § 4.2, we choose $\epsilon=(Re/\Gamma)^{1/2}$ as the small parameter of the asymptotic analysis. This is equivalent to assuming $Re\ll 1$ because $\Gamma\sim O(1)$ for the unstable modes

mentioned in preceding discussion. As per the numerical scalings shown in figure 4, we assume that $\Gamma \sim O(1), k = k_0\epsilon$ where $k_0 \sim O(1)$ is the scaled non-dimensional wavenumber and the complex wave speed is expanded in a series as

$$c = \frac{1}{\epsilon^2}\left(c^{(0)} + \epsilon c^{(1)} + \cdots\right). \tag{B 1}$$

If we set $\tilde{v}_z \sim O(1)$, then $\tilde{v}_x \sim O(\epsilon^{-1})$ and $\tilde{p} \sim O(\epsilon^{-2})$ according to the fluid continuity equation (3.9) and x-momentum balance (3.10), respectively. Thus, the velocities and pressure in fluid are expanded as

$$\tilde{v}_z = \tilde{v}_z^{(0)} + \epsilon\tilde{v}_z^{(1)} + \epsilon^2\tilde{v}_z^{(2)} + \cdots, \tag{B 2}$$

$$\tilde{v}_x = \epsilon^{-1}\left(\tilde{v}_x^{(0)} + \epsilon\tilde{v}_x^{(1)} + \epsilon^2\tilde{v}_x^{(2)} + \cdots\right), \tag{B 3}$$

$$\tilde{p} = \epsilon^{-2}\left(\tilde{p}^{(0)} + \epsilon\tilde{p}^{(1)} + \epsilon^2\tilde{p}^{(2)} + \cdots\right). \tag{B 4}$$

The normal velocity continuity condition indicate that $\tilde{w}_Z \sim O(\epsilon)$ at $z = 0$. We assume $\tilde{w}_Z \sim O(\epsilon)$ in the bulk of solid medium as well, and thus solid continuity (3.12) and x-momentum balance (3.13) imply that $\tilde{w}_X \sim O(1)$ and $\tilde{p}_s \sim O(\epsilon^{-1})$, respectively. The deformation and pressure fields in solid are then expanded as

$$\tilde{w}_Z = \epsilon\left(\tilde{w}_Z^{(0)} + \epsilon\tilde{w}_Z^{(1)} + \cdots\right), \tag{B 5}$$

$$\tilde{w}_X = \left(\tilde{w}_X^{(0)} + \epsilon\tilde{w}_X^{(1)} + \cdots\right), \tag{B 6}$$

$$\tilde{p}_s = \epsilon^{-1}\left(\tilde{p}_s{}^{(0)} + \epsilon\tilde{p}_s{}^{(1)} + \cdots\right). \tag{B 7}$$

The above expansions for fluid eigenfunctions (B 2)–(B 4), solid eigenfunctions (B 5)–(B 7) and $k = k_0\epsilon$ are substituted in the governing equations (3.9)–(3.14) and the boundary conditions (3.15)–(3.21) to obtain a set of equations governing the problem at different orders in ϵ.

Subsequent analysis reveals that we require fluid eigenfunctions correct to $O(\epsilon^2)$ and solid eigenfunctions correct to $O(\epsilon)$ in order to determine the stability of the system. The eigenfunctions for fluid at different orders in ϵ, i.e. $O(\epsilon^0)$, $O(\epsilon^1)$ and $O(\epsilon^2)$, are obtained by substituting the expansions (B 2)–(B 4) in the governing equations of fluid (defined in (3.9)–(3.11)) and solving the resulting equations at respective orders in ϵ. Similarly, the solid eigenfunctions correct to $O(\epsilon)$ are obtained by substituting the expansions (B 5)–(B 7) in the solid governing equations (defined in (3.12)–(3.14)) and solving the resulting equations at $O(\epsilon^0)$ and $O(\epsilon)$. The fluid and solid eigenfunctions, thus obtained, are substituted in boundary conditions (3.15)–(3.21). This results in a system of linear homogeneous equations which can be represented as

$$\boldsymbol{M}\cdot\boldsymbol{C}^{\boldsymbol{T}} = 0, \tag{B 8}$$

where $\boldsymbol{C}$ is the vector of constants: $\{A_1, A_2, A_3, A_4, G_1, G_2, G_3, G_4\}$. A_i and G_i $(i = 1\text{–}4)$ are the constants occurring in fluid and solid eigenfunctions, respectively. The characteristic equation is obtained by setting $\det[\boldsymbol{M}] = 0$ and this determinant is expanded in series of ϵ as follows:

$$f_0\left(c^{(0)}\right) + \epsilon f_1\left(c^{(0)}, c^{(1)}\right) + \cdots = 0, \tag{B 9}$$

where f_0 is the leading-order term in the determinant and f_1 is the first correction. The leading-order term, first correction and higher-order terms must be separately zero for the determinant to be zero. The condition of vanishing of leading-order determinant i.e. $f_0(c^{(0)}) = 0$ determines the leading-order wave speed and it shows that there are multiple solutions for $c^{(0)}$ all of which are real, and could be positive or

negative. This indicates that, to the leading-order approximation, the perturbations are neutrally stable waves travelling in both upstream (with $c^{(0)}$ negative) and downstream directions (with $c^{(0)}$ positive).

Because the system is neutrally stable up to this order of approximation, it is necessary to calculate the next correction to the wave speed $c^{(1)}$ in order to determine the stability of the system. The $O(\epsilon)$ correction of determinant is used to evaluate $c^{(1)}$ and it turns out that $c^{(1)}$ is purely imaginary. The flow is stable (unstable) if $c^{(1)} < 0$ ($c^{(1)} > 0$). As mentioned above, there are multiple solutions for $c^{(0)}$ and these can be either with positive (downstream modes) or negative signs (upstream modes). For each of these $c^{(0)}$, there is a unique first correction $c^{(1)}$ which determines the stability of that particular mode. The expression for $c^{(1)}$ shows that the upstream travelling waves become unstable when Γ is increased above a critical value. On the other hand, the downstream travelling modes do not become unstable for any value of Γ. In fact, increasing Γ has a stabilizing effect on downstream travelling waves. The condition $c^{(1)} = 0$ (for upstream travelling modes) can be used to solve for Γ required for destabilizing the flow. We have compared the results obtained from the asymptotic analysis with the numerical results presented in figure 4 and found that they are in excellent agreement with each other for $Re \ll 1$. We have further verified that the scaling assumptions made in the asymptotic analysis for various dynamical quantities are consistent with the numerical solution. Recall that the upstream modes were labelled 'Var-1u', 'Var-2u' and so on, in increasing order of their wave speeds, and the slowest upstream travelling mode becomes unstable first with increase in Γ. The asymptotic results also confirm that the first upstream mode is most easily destabilized with increase in fluid velocity Γ. It is important to remark here that the instability of upstream travelling modes for low Reynolds number and low wavenumber was not observed in earlier works related to the stability of flow past a deformable surface (Kumaran *et al.* 1994; Kumaran 1995; Srivatsan & Kumaran 1997; Shankar & Kumaran 2000) where the deformable wall was modelled as linear viscoelastic solid. Thus, the low-Re and low-k upstream mode instability analysed here is a consequence of the additional coupling terms between the base state of solid and perturbation variables (boxed terms in (3.12)–(3.14) and (3.17)–(3.18)) present for a neo-Hookean solid model.

Importantly, the asymptotic analysis indicates that the leading-order perturbation velocity in the fluid has a plug-flow velocity profile. This perturbation velocity is possible only if both the walls allow for a non-zero tangential fluid velocity, as is the case here as well as in the tube flow of Gaurav & Shankar (2009). If one of the walls is rigid, then the fluid disturbance velocity must be zero there, and this precludes the possibility of the low-k instability predicted here. Hence, this new class of modes would be absent for the plane Couette flow (Gkanis & Kumar 2003) and in two of the configurations considered by Gkanis & Kumar (2005).

REFERENCES

Achenbach, D. J. 1973 *Wave Propagation in Elastic Solids*. North-Holland.

Beatty, M. F. & Zhou, Z. 1991 Universal motion for a class of viscoelastic materials of differential type. *Contin. Mech. Thermodyn.* **3**, 169–191.

Benjamin, T. B. 1960 Effect of a flexible surface on boundary layer stability. *J. Fluid Mech.* **9**, 513–532.

Boyd, J. P. 1989 *Chebyshev and Fourier Spectral Methods*. Springer.

Chokshi, P. 2007 Studies in the stability of newtonian and viscoelastic flows past rigid and flexible surfaces. PhD thesis, Indian Institute of Science, Bangalore, India.

Choskshi, P. & Kumaran, V. 2008 Weakly nonlinear analysis of viscous instability in flow past a neo-Hookean surface. *Phys. Rev.* E **77**, 056303.

Davies, C. & Carpenter, P. W. 1997 Instabilities in a plane channel flow between compliant walls. *J. Fluid Mech.* **352**, 205–243.

Destarde, M. & Saccomandi, G. 2004 Finite-amplitude inhomogeneous waves in Mooney–Rivlin viscoelastic solids. *Wave Motion* **40**, 251–262.

Drazin, P. G. 2002 *Introduction to Hydrodynamic Stability*. Cambridge University Press.

Drazin, P. G. & Howard, L. N. 1966 Hydrodynamic stability of parallel flow of a inviscid fluid. In *Advances in Applied Mechanics* (ed. G. G. Chernyi), vol. 9, pp. 1–90. Academic Press.

Drazin, P. G. & Reid, W. H. 1981 *Hydrodynamic Stability*. Cambridge University Press.

Eggert, M. D. & Kumar, S. 2004 Observations of instability, hysterisis, and oscillation in low-Reynolds number flow past polymer gels. *J. Colloid Interface Sci.* **274**, 234–242.

Fosdick, R. L. & Yu, J. H. 1996 Thermodynamics, stability and non-linear oscillations of viscoelastic solids. Part I. Differential type solids of second grade. *Intl J. NonLinear Mech.* **31**, 495–516.

Gad-el-Hak, M. 2003 Drag reduction using compliant walls. In *IUTAM Symposium on Flow Past Highly Compliant Boundaries and in Collapsible Tubes* (ed. P. W. Carpenter & T. J. Pedley), chap. 9, pp. 191–229. Kluwer Academic.

Gajjar, J. S. B. & Sibanda, S. K. 1996 The hydrodynamic stability of channel flow with compliant boundaries. *Theor. Comput. Fluid Dyn.* **8**, 105–129.

Gaurav & Shankar, V. 2007 Stability of gravity-driven free-surface flow past a deformable solid layer at zero and finite Reynolds number. *Phys. Fluids* **19**, 024105.

Gaurav & Shankar, V. 2009 Stability of fluid flow through deformable neo-Hookean tubes. *J. Fluid Mech.* **627**, 291–322.

Gkanis, V. & Kumar, S. 2003 Instability of creeping Couette flow past a neo-Hookean solid. *Phys. Fluids* **15**, 2864–2471.

Gkanis, V. & Kumar, S. 2005 Stability of pressure-driven creeping flows in channels lined with a nonlinear elastic solid. *J. Fluid Mech.* **524**, 357–375.

Green, C. H. & Ellen, C. H. 1972 The stability of plane Poiseuille flow between flexible walls. *J. Fluid Mech.* **51**, 403–416.

Grotberg, J. B. & Jensen, O. E. 2004 Biofluid mechanics in flexible tubes. *Annu. Rev. Fluid Mech.* **36**, 121–147.

Hains, F. D. & Price, J. F. 1962 Effect of flexible wall on stability of Poiseuille flow. *Phys. Fluids* **5**, 365.

Holzapfel, G. A. 2000 *Nonlinear Solid Mechanics*. Wiley.

Huang, L. 1998 Reversal of the Bernoulli effect and channel flutter. *J. Fluids Struct.* **12**, 131–151.

Huerre, P. & Rossi, M. 1998 Hydrodynamic instabilities in open flows. In *Hydrodynamics and Nonlinear Instabilities* (ed. C. Goodreche & P. Manneville), chap. 2, pp. 95–118. Cambridge University Press.

Krindel, P. & Silberberg, A. 1979 Flow through gel-walled tubes. *J. Colloid Interface Sci.* **71**, 34–50.

Kumaran, V. 1995 Stability of the viscous flow of a fluid through a flexible tube. *J. Fluid Mech.* **294**, 259–281.

Kumaran, V. 1998 Stability of fluid flow through a flexible tube at intermediate Reynolds number. *J. Fluid Mech.* **357**, 123–140.

Kumaran, V., Fredrickson, G. H. & Pincus, P. 1994 Flow induced instability of the interface between a fluid and a gel at low Reynolds number. *J. Phys.* II *France* **4**, 893–904.

Kumaran, V. & Muralikrishnan, R. 2000 Spontaneous growth of fluctuations in the viscous flow of a fluid past a soft interface. *Phys. Rev. Lett.* **84**, 3310–3313.

Landahl, M. T. 1962 On the stability of a laminar incompressible boundary layer over a flexible surface. *J. Fluid Mech.* **13**, 609–632.

LaRose, P. G. & Grotberg, J. B. 1997 Flutter and long-wave instabilities in compliant channels conveying developing flows. *J. Fluid Mech.* **331**, 37–58.

Ma, Y. & Ng, C.-O. 2009 Wave propagation and induced steady streaming in viscous fluid contained in a prestressed viscoelastic tube. *Phys. Fluids* **21**, 051901.

Malvern, L. E. 1969 *Introduction to the Mechanics of a Continuous Medium*. Prentice-Hall.

Mandre, S. & Mahadevan, L. 2010 A generalized theory of viscous and inviscid flutter. *Proc. R. Soc.* A **466**, 141–156.

McDonald, J. C. & Whitesides, G. M. 2002 Poly(dimethylsiloxane) as a material for fabricating microfluidic devices. *Acc. Chem. Res.* **35**, 491–499.

Muralikrishnan, R. & Kumaran, V. 2002 Experimental study of the instability of viscous flow past a flexible surface. *Phys. Fluids* **14**, 775–780.

Nagata, M. & Cole, T. R. 1999 On the stability of plane Poiseuille flow between compliant boundaries. In *Proceedings of International Conference of Computational Methods and Experimental Measurements IX,* Naples, Italy (ed. G. M. Carlomagno & C. A. Brebbia), pp. 231–240. WIT Press.

Rotenberry, J. M. & Saffman, P. G. 1990 Effect of compliant boundaries on the weakly nonlinear shear waves in a channel flow. *SIAM J. Appl. Math.* **50**, 361–394.

Schmid, P. 2007 Nonmodal stability theory. *Annu. Rev. Fluid Mech.* **39**, 129–162.

Schmid, P. J. & Henningson, D. S. 2001 *Stability and Transition in Shear Flows*. Springer.

Shankar, V. 2004 Stability of two-layer viscoelastic plane Couette flow past a deformable solid layer. *J. Non-Newton. Fluid Mech.* **117**, 163–182.

Shankar, V. & Kumaran, V. 2000 Stability of fluid flow in a flexible tube to non-axisymmetric disturbances. *J. Fluid Mech.* **408**, 291–314.

Shankar, V. & Kumaran, V. 2001 Asymptotic analysis of wall modes in a flexible tube revisited. *Eur. Phys. J.* B **19**, 607–622.

Shankar, V. & Kumaran, V. 2002 Stability of wall modes in fluid flow past a flexible surface. *Phys. Fluids* **14**, 2324–2338.

Shrivastava, A., Cussler, E. L. & Kumar, S. 2008 Mass transfer enhancement due to a soft elastic boundary. *Chem. Engng Sci.* **63**, 4302–4305.

Squires, T. M. & Quake, S. R. 2005 Microfluidics: fluid physics at the nanoliter scale. *Rev. Mod. Phys.* **77**, 977–1026.

Srivatsan, L. & Kumaran, V. 1997 Stability of the interface between a fluid and gel. *J. Phys.* II. *France* **7**, 947–963.

Stewart, P. S., Walters, S. L. & Jensen, O. E. 2010 Local instabilities of flow in a flexible channel: asymmetric flutter driven by a weak critical layer. *Phys. Fluids* **22**, 031902.

Thomas, M. S., Clift, J. M., Millare, B. & Vullev, V. I. 2010 Print-and-peel fabricated passive micromixers. *Langmuir* **26**, 2951–2957.

Verma, M. K. S, Ganneboyina, S. R., Rakshith, R. V. & Ghatak, A. 2008 Three-dimensional multihelical microfluidic mixers for rapid mixing of liquids. *Langmuir* **24**, 2248–2251.

Weideman, J. A. & Reddy, S. C. 2000 A Matlab differentiation matrix suite. *ACM Trans. Math. Softw.* **26**, 465–519.

Yeo, K. S. 1988 The stability of boundary layer flow over single and multilayer viscoelastic walls. *J. Fluid Mech.* **196**, 359–408.

Yeo, K. S., Khoo, B. C. & Chong, W. K. 1994 The linear stability of boundary layer flow over compliant walls: the effects of wall mean state induced by flow loading. *J. Fluids Struct.* **8**, 529–551.